2022-12-01

Infiltration-Controlled Combustion of Lithium and Magnesium Powders and Reactions of Lithium With Oxygen and Carbon Dioxide

Kevin Samuel Estala Rodriguez
University of Texas at El Paso

INFILTRATION-CONTROLLED COMBUSTION OF LITHIUM AND MAGNESIUM POWDERS AND REACTIONS OF LITHIUM WITH OXYGEN AND CARBON DIOXIDE

KEVIN SAMUEL ESTALA RODRIGUEZ

Doctoral Program in Mechanical Engineering

APPROVED:

Evgeny Shafirovich, Ph.D., Chair

Md Mahamudur Rahman, Ph.D.

Brian E. Schuster, Ph.D.

Stephen L. Crites, Jr., Ph.D.
Dean of the Graduate School

Dedication

To my family, for believing in me and for giving me their support. To my fiancé, for pushing me to achieve my goals.

In loving memory of my mom.

INFILTRATION-CONTROLLED COMBUSTION OF LITHIUM AND MAGNESIUM POWDERS AND REACTIONS OF LITHIUM WITH OXYGEN AND CARBON DIOXIDE

by

KEVIN SAMUEL ESTALA RODRIGUEZ, BSME, MSME

DISSERTATION

Presented to the Faculty of the Graduate School of

The University of Texas at El Paso

in Partial Fulfillment

of the Requirements

for the Degree of

DOCTOR OF PHILOSOPHY

Department of Aerospace and Mechanical Engineering

THE UNIVERSITY OF TEXAS AT EL PASO

December 2022

Acknowledgements

First, I would like to praise and thank God, especially for giving the strength and encouragement through my studies and putting the right people to help me achieve my goals.

I would like to thank my advisor Dr. Shafirovich, for giving me the opportunity to work with him and learn from him. For his patience and guidance through all my PhD studies. And for all the travel experiences. To my labmates Sergio, Robert, Alan, Frank, and Reina, for taking the time to teach me and guide me.

Special thanks to my labmates Dominic, Victoria, and Zachary for making this last year a memorable one.

I would like to acknowledge NASA's Space Technology Research Grants Program for the Early Stage Innovations grant (Grant #80NSSC20K0293) which supported this work.

Abstract

Chemical heat integrated power systems are of great interest for space missions where solar energy, nuclear energy, and batteries are not available or are not practical to use. A new concept of a power system is a metal combustor coupled with a chemical oxygen generator, where the generated oxygen infiltrates through the metal powder or combustion products. The combustion of lithium and magnesium powders under these conditions has not been studied yet. The present work investigates combustion of magnesium powder and stabilized lithium metal powder (SLMP) ignited by a laser inside a closed chamber filled with O_2 or CO_2. It also includes experimental studies on the reactions of SLMP with O_2 and CO_2 by using non-isothermal and isothermal methods of thermogravimetric analysis (TGA) and differential scanning calorimetry (DSC).

The combustion of Mg and Li powders in vertical quartz tubes at natural infiltration of oxygen has been demonstrated at atmospheric or lower pressure. It has been shown that laser ignition of either powder leads to a counterflow combustion wave at low conversion. This process is followed by a backward coflow combustion wave or, in some tests with Li, by a continued reaction of the entire sample. In CO_2, self-sustained combustion did not occur, apparently because of formation of byproducts that hinder CO_2 transportation to the reaction zone.

During oxidation in both O_2 and CO_2 environments, Li powder reacted mainly after melting, leading to the formation of hollow spheres. Oxidation by O_2 to Li_2O involves transition from a slow to a faster stage, which is explained by formation and decomposition of Li_2O_2. In CO_2, Li is first oxidized to Li_2O, which is then converted into Li_2CO_3. High-pressure DSC has shown that the increase in pressure from 10 to 30 bar promotes the conversion of the sample into Li_2CO_3.

Table of Contents

List of Tables

List of Figures

Chapter 1: Introduction

As the solar system exploration rapidly increases, the technological development or enhancement of power systems to sustain space missions is required. Specifically, where solar energy is not available, and batteries become impractical to use. Nuclear energy is also not ideal due to restrictions associated with launching and costs. As a result, there is a growing interest in chemical heat integrated power systems (CHIPS) which rely on chemical reactions to provide heat and power to spacecraft. One example of this technology is a power system in development with the goal of surviving a cold and long lunar night, which uses lithium (Li) and sulfur hexafluoride (SF_6) as the reactants [1-3]. This system is approximated to have a specific energy of 14.6 MJ/kg of the reactants. Another example is the batch reactor that utilizes the reaction of lithium and carbon dioxide (CO_2) in order to produce power and to cool down a Venus lander [4]. An important aspect that can bring more interest into this technology is the use of in situ resources, such as CO_2 as an oxidizer, which leads to a higher specific energy of the system.

Recently, it was proposed to use lithium and magnesium (Mg) powders as metal fuels to react with oxygen in order to provide large amounts of heat and power relying on a process commonly called “filtration combustion” and used for synthesis of transition metal nitrides and hydrides. In this process, a gaseous reactant infiltrates to the reaction zone through the bed of the initial metal powder or the combustion products, thus enabling self-sustained propagation of the combustion wave over the metal powder. However, the filtration combustion of lithium and magnesium has not been studied yet. The present work focuses on the experimental validation of the filtration combustion of Mg and Li powders in O_2 and CO_2 environments inside a closed chamber. The process relies on the natural infiltration of the gaseous oxidizer due to a pressure gradient that forms as a result of consuming the gas in the reaction zone.

As the oxidation process of the metal is fundamental to understand the combustion process, the present work also includes experimental studies on the reactions of lithium with O_2 and CO_2. Recently, the oxidation kinetics of magnesium has been studied by non-isothermal and isothermal methods of thermogravimetric analysis (TGA), which determined the apparent activation energy and kinetic models of spherical and irregularly shaped Mg powders [5]. However, there are no data on the oxidation of a stabilized lithium metal powder (SLMP), which recently became commercially available. The present work investigates the oxidation of this powder in O_2 and CO_2 by non-isothermal and isothermal TGA and differential scanning calorimetry analysis (DSC) at atmospheric pressure. In addition, since the atmospheric pressure near the surface of Venus is as high as 92 bar, the effect of pressure on the Li-CO_2 reaction is studied using high-pressure DSC.

Chapter 2: Infiltration-controlled Combustion of Magnesium for Power Generation in Space

2.1 INTRODUCTION

Solar arrays and radioisotope thermoelectric generators have been used extensively to generate power in space missions. However, many of the currently designed missions cannot rely on these power sources, and batteries cannot replace them because of low specific energy and limited lifetime. There is a growing interest in power systems based on the heat of exothermic chemical reactions (the so-called chemical heat integrated power systems [1-3]). Many fuel-oxidizer combinations have a very high specific energy as compared to those of the best batteries. However, only some of them satisfy another important criterion: easy storage, which requires the solid or liquid state of the reactants under normal conditions. If dense reactants can be stored for a long time with no loss of energy, the system will have a great advantage over batteries. In addition, since only part of heat can be converted to electric power, the combustion-based system will be especially attractive for space missions where there is a need not only for electric power but also for heat to maintain the required temperature regime in the lander or spacecraft.

The feasibility of using solid reactive mixtures for heat generation in power systems has been explored previously. Specifically, the researchers studied combustion of Ti/C, Ti/B, and $Fe_2O_3/TiO_2/Al/C$ mixtures, which exhibit exothermic reactions between the components and have specific energies of 3.1, 4.0, and 3.2 MJ/kg, respectively [6-8]. The advantage of this approach is the solid state of the reactants and products. However, the specific energies of the mixtures are relatively low. The state-of-the-art primary battery technology provides 200 – 300 Wh/kg (0.72 – 1.08 MJ/kg) [1-3]. Taking into consideration the thermal efficiency of the heat-to-electricity

conversion and the mass of structural components, the combustion of these mixtures would provide less electric energy than modern batteries could.

One promising combustible system with condensed reactants is lithium and sulfur hexafluoride (Li – SF_6). This system has been used in underwater propulsion systems to provide heat for the Rankine cycle [9]. SF_6 can be stored as a saturated liquid with a vapor pressure of 22 bar at 294 K [10]. The reaction produces condensed compounds LiF and Li_2S, which occupy less space than the lithium did. The Li-SF_6 system has a rather high specific energy, 14.1 MJ/kg [11]. Recently, it has been proposed to use it as an energy source in Venus and Europa surface missions [10-11] as well as in a lunar night survival mission [1-3]. Specifically, the lithium, stored as a solid, will be melted before the operation and either react at the surface or pulled by capillary forces over the wick toward the gas-phase reaction zone. The condensed compounds will sink in the molten Li, so they will not impede the process. Note that any design for the Li-SF_6 system involves gravity, which is absent or very small in many space applications.

An alternative approach is to use the combustion of metal powders with oxygen, which could be stored in chemical oxygen generators. These devices (also called solid-state oxygen generators, self-contained oxygen generators, or oxygen candles) are widely used in aircraft, submarines, space stations, and fire safety applications. Chemical oxygen generators usually contain sodium chlorate ($NaClO_3$) or lithium perchlorate ($LiClO_4$) as the oxygen source and small amounts of a metal fuel (typically iron), a catalyst, and other ingredients [12]. They do not require any maintenance during a long (many years) lifetime. The use of chemical oxygen generators in long-term space missions appears to be advantageous over compressed gaseous or liquid oxygen [13].

The combustion process in the proposed concept is the so-called filtration combustion of metals [14, 15]. It is envisioned that a cylindrical reactor is filled with a combustible metal powder, and a gaseous reactant is fed into the reactor from one end ("forced infiltration" [15]). The combustion wave propagation is initiated by ignition at either the same end or the opposite one. The former leads to the coflow regime, where the oxidizing gas infiltrates through the combustion products, while the latter leads to the counterflow combustion, where the gas infiltrates through the initial powder. The system can include several heat-generating cartridges, each with a chemical oxygen generator and a metal combustor, to provide power during a long mission.

Among the potential metal fuels, magnesium appears to be a promising one. The overall reactions of $NaClO_3$ and $LiClO_4$ decomposition and Mg oxidation are described by the equations:

$$3\ Mg + NaClO3 \rightarrow 3\ MgO + NaCl \tag{2.1}$$

$$4\ Mg + LiClO4 \rightarrow 4\ MgO + LiCl \tag{2.2}$$

The specific energies of Mg-$NaClO_3$ and Mg-$LiClO_4$ systems are 10.3 and 11.9 MJ/kg, respectively, i.e., they are not much lower than that of the Li-SF_6 system (here the enthalpies of formation at standard conditions were taken from [16] for NaClO3 and from [17] for the other compounds). Since the Pilling-Bedworth ratio (the ratio of the volume of a metal oxide to the volume of the metal from which the oxide is created [18]) is 0.81 for Mg in oxygen, the magnesia (MgO) produced by its combustion will occupy less space than the initial Mg powder did, which enables the coflow regime and does not require additional space in the reactor. The high melting point of MgO, 2852 °C, indicates that the combustion products will not be melted or sintered into

an impermeable mass, which would preclude the coflow combustion. For comparison, aluminum, while advantageous energetically, has a Pilling-Bedworth ratio of 1.28, and the melting point of Al_2O_3 is only 2072 °C.

The filtration combustion has been used for self-propagating high-temperature synthesis (SHS) of various metallic and nonmetallic nitrides and hydrides [14.15]. An important criterion in filtration combustion is the ratio of the characteristic time of infiltration to the characteristic time of reaction. If the infiltration is slow, the combustion wave can propagate only if the amount of the reactive gas in the pores is sufficient for at least partial conversion. In practice, SHS of nitrides was conducted at pressures over 1000 bar to have sufficient nitrogen in the pores [14,15].

Modeling of the filtration combustion has revealed interesting behaviors such as counterflow combustion with incomplete conversion of the solid reactant followed by the backward propagation of a second combustion wave [19-21], splitting of the reaction front into two separately propagating fronts [22-24], superadiabatic combustion temperatures [24,25], and spinning combustion waves [26,27]. Such phenomena have also been observed in the experiments. For example, counterflow combustion of a tantalum powder with nitrogen at pressures of 20 – 100 bar resulted in a second combustion front propagating backward [28]. It should be noted, however, that in many modeling and experimental papers, the initial gas pressure in pores was sufficiently high for complete conversion (of the order of 1000 bar). In the proposed combustors for space power systems, the gas pressure is relatively low and the infiltration should be sufficiently rapid to provide enough gas for the reaction. The combustion under these conditions has been studied less.

The objective of the present work was to investigate the combustion of a magnesium powder at “natural infiltration” [14], where the gas pressure in the environment is low and oxygen

penetrates because of the pressure difference caused by the consumption of oxygen in the reaction zone. If the combustion at such a low pressure difference is possible, it can be expected that combustion in practical devices with forced infiltration of the gaseous oxidizer will be effective.

2.2 MATERIALS AND METHODS

A magnesium powder (99.8% pure, –325 mesh) was obtained from MilliporeSigma. The morphology of Mg particles was examined with a scanning electron microscope (SEM Hitachi S-4800). Figure 2.1 shows the SEM images of the particles. It is seen that particles have an irregular shape.

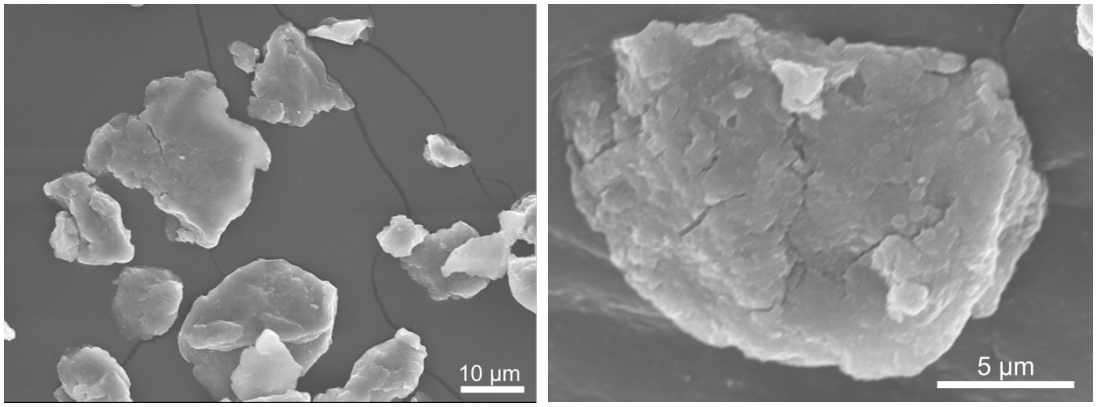

Figure 2.1: SEM images of the Mg particles.

Figure 2.2 shows the particle size distribution of the powder, determined using a laser diffraction particle size analyzer (Microtrac Bluewave) and isopropyl alcohol as a liquid carrier. The statistical parameters of the powder distribution are 31 µm, 23 µm, and 28 µm for the volume mean diameter, the Sauter mean diameter, and the median diameter, respectively.

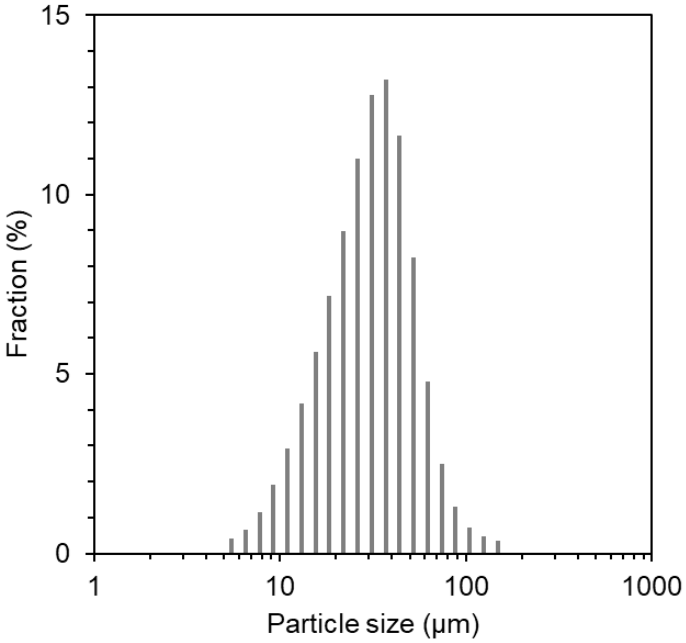

Figure 2.2: Particle size distribution of the Mg powder.

The bulk density of each sample was determined by measuring the mass and volume of the powder in the quartz tube before the experiment. The obtained values of the porosity were in the range from 68.3 to 73.6%. The variations of the bulk density and hence porosity were unavoidable in the used method of loading the powder into the tube. Densification of the powder in the tube using a shaker (Gilson SS-28 Vibra Pad) decreased the porosity to about 60%. However, in the experiments with the densified powder, only the top layer of the powder burned. Therefore, all combustion experiments reported here were conducted with the powder that was not densified.

The combustion experiments were conducted in a laser ignition setup, previously used for experiments with reactive mixtures [29-32]. The setup includes a stainless-steel vacuum chamber (volume: 11.35 L) connected to a vacuum pump and a compressed gas cylinder. It is equipped with two window-door ports and two windows, one of which was made of sapphire to enable infrared video recording. The ignition system includes a CO_2 laser (Synrad Firestar ti-60), an

infrared beam of which (wavelength: 10.55 – 10.68 μm, diameter: 2.0 ± 0.3 mm) enters the chamber vertically through a zinc selenide window in the lid. The power of the beam was measured with a powermeter (Synrad PW-250) and controlled by a laser controller (Synrad UC-2000), while the duration of the laser pulse was set using LabVIEW (National Instruments) software connected to the laser controller. In the experiments reported in the present paper, the power of the beam after passing the zinc selenide window was 32 W, while the laser pulse duration was 125 ms.

The experiments were conducted in O_2 (purity 99.994%, Airgas) at absolute pressures of 330 – 675 Torr (44 – 90 kPa). Higher pressures were not tested because the chamber was not designed to exceed the atmospheric pressure (about 90 kPa in El Paso, TX). The absolute pressure in the chamber was measured by a Pirani capacitance diaphragm vacuum gauge (Inficon PCG554).

Quartz tubes (inne`r diameter: 7 mm, outer diameter: 9 mm, length: 50 mm) were used to hold the Mg powder during the experiment. The tube was installed vertically in a stainless-steel holder, several alumina tubes (length: 10 mm, outer diameter: 1.0 and 1.6 mm) were installed vertically at the bottom of the quartz tube, and a thin layer of thermal insulation paper (Fiberfrax) was placed on top of the alumina tubes to support the metal powder. The alumina tubes were used to locate the bottom of the powder sample above the top of the steel holder so that the whole sample could be seen. The quartz tube was then filled with the tested Mg powder to a bed height of approximately 38 mm, and the holder with the tube was installed on a brass pedestal inside the chamber. The infrared beam of the CO_2 laser was aligned with the center of the top end of the sample using a red beam of a laser diode pointer (Synrad), pre-aligned with the infrared beam.

Before the experiment, the chamber was evacuated and filled with argon three times. Then, the argon was evacuated until the absolute pressure decreased to 1 – 1.5 Torr, and the chamber

was filled with O_2 at the desired pressure. This procedure resulted in an O_2 mole fraction of 0.998 – 0.999 for 90 kPa and 0.995 – 0.997 for 44 kPa.

The combustion process was recorded at 500 fps with a high-speed camera (Vision Research Phantom v1210), equipped with a lens for macro shooting (Nikon AF Micro NIKKOR 60 mm f/2.8D). An infrared video camera (FLIR SC7650E, spectral range: 1.5 – 5.1 μm) was used to observe the propagation of a thermal wave when no visible light was emitted as well as to provide additional information on the propagation of combustion waves. The calibrations of the camera for 0–300 °C and 300–1500 °C were used, and the recording was conducted at 50 fps.

In several experiments, one to three thermocouples (Chromel/Alumel, type K, wire diameter: 80 μm, Omega Engineering) were used to measure the temperature in the sample during the combustion process. The thermocouples, located in two-channel ceramic insulators (outer diameter: 1.24 mm, Omegatite 450, Omega Engineering), were inserted into the powder perpendicularly to the axis through the holes drilled in the quartz tube. The gaps between the ceramic insulators and quartz as well as the channels in the insulators were sealed with an electrically resistant ceramic adhesive (2800°F-RESBOND 919, Cotronics). The thermocouples were connected to a data acquisition system (National Instruments USB-9211) for recording at 100 Hz.

The extent of conversion was determined by the measurements of the initial and final masses of the sample with a balance, assuming that the extent of conversion is equal to 1 when the ratio of these masses is equal to the ratio of molar masses of Mg and MgO (in the tested powder, the mass of the oxide film is negligible compared to the mass of the particle). The combustion products were analyzed with the aforementioned scanning electron microscope.

2.3 RESULTS AND DISCUSSION

Figure 2.3 shows images of a typical combustion process at 90 kPa. In the first image (Fig. 2.3a), the laser heats the top layer of the powder. After the ignition, the combustion front propagates downward, but only over a short distance. Figure 2.3b shows where the front stopped. The quenching can be explained as follows. With the abundant O_2 near the top surface, the combustion of the top layer generates very high temperatures (the adiabatic flame temperature of the stoichiometric Mg/O_2 mixture well exceeds the MgO melting point, 2852 °C). This leads to the melting and sintering of underlying Mg particles into an impermeable layer, which was confirmed by analysis of a quenched sample. The combustion of the top layer sucks oxygen from the pores between the underlying particles, but at the tested gas pressures, the amount of oxygen in the pores is very small, so the combustion is ceased quickly. Since the pressure inside the sample dropped, oxygen penetrates into the tube through a gap between the tube and the holder, and then through the supporting structure at the bottom of the tube. The pressure difference pushes the powder upward, and a gap appears between the powder and the supporting material (Figs. 2.3b and 2.3c).

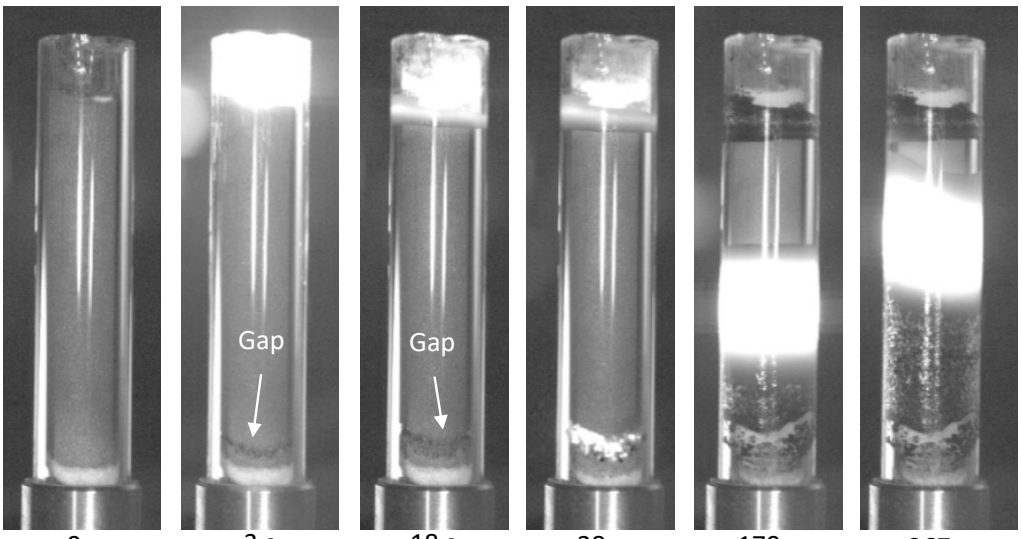

Figure 2.3: Combustion of Mg powder in oxygen at 90 kPa. Time is relative to the laser pulse.

Meanwhile, a heat wave propagates downward over the powder and the quartz tube. This propagation is clearly seen in the infrared images shown in the top row in Figure 2.4. It should be noted that the infrared recording in the present work was not used for the determination of actual temperatures, the emissivity was simply assumed to be 1, and the temperature values shown in Fig. 2.4 differ from the actual temperatures. The temperature rise at the bottom leads to the ignition in the gap (Fig. 2.3d). Next, the combustion wave forms and slowly propagates upward (Figs. 2.3e and 2.3f) until it reaches the top layer of the sample, which has already been oxidized. The upward propagation of the combustion wave is also clearly seen in the infrared images (Fig. 2.4, the bottom row).

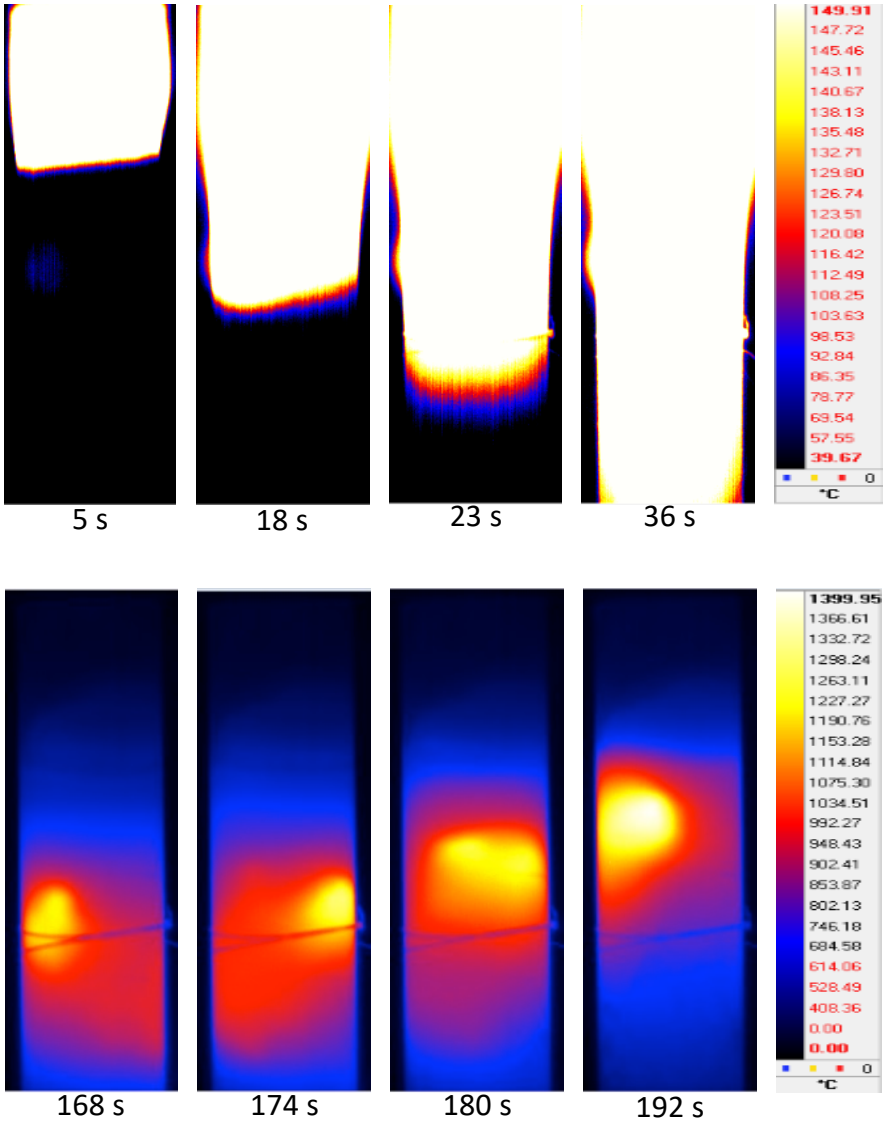

Figure 2.4: Infrared images of heat propagation after laser ignition (top row) and after ignition at the bottom (bottom row) during combustion of Mg powder in oxygen at 90 kPa.

Analysis of the infrared video records clearly shows a spinning propagation of the combustion front upward: the zone of the highest temperature travels along a helical path. This indicates an oscillatory instability of the planar front. It is known that, depending on the dimensions and geometry of the sample, the oscillatory instability of the planar combustion wave can result in different propagation modes such as one-dimensional pulsations, a spinning wave, and multi-point combustion. For example, in the work [33], the origin of the spinning wave was attributed to

asynchronous one-dimensional pulsations of different parts of the front. The spinning combustion waves have been observed for powdered transition metals such as titanium, zirconium, hafnium, and tantalum, compacted and ignited in a nitrogen environment. The first experiments were conducted at nitrogen pressures as high as dozens of bars, but later the experiments were also performed at pressures lower than 1 bar [34-38]. All those experiments were conducted with pressed cylindrical samples, where the nitrogen infiltrated through the lateral surface (perpendicularly to the axis) and the reaction occurred mainly in the surface layer. The formation of spinning combustion waves under such conditions was simulated in a three-dimensional mathematical model of filtration combustion [24,25]. However, to our knowledge, the oscillatory instability of the flame front has not been observed yet for metal powder samples with an impermeable lateral surface where the gaseous oxidizer is a deficient component that enters the sample at the end and infiltrates along the axis.

In the present work, the penetration of oxygen from the bottom end was confirmed in the experiments where the bottom of the tube was closed by a 10 mm layer of the same ceramic adhesive that was used for sealing the thermocouple ports (the adhesive was placed instead of the alumina tubes, see Figure A1). In this case, only the top layer burned.

The propagation of the thermal wave downward followed by the propagation of the thermal wave upward was also confirmed by temperature measurements with three thermocouples inserted into the powder at 10, 20, and 30 mm from the top surface of the powder. Figure 2.5 shows that each temperature profile has two peaks. The first peak indicates propagation of the thermal wave downward, while the second peak is caused by the upward propagation of the second thermal wave. The maximum temperature of the first peak slightly exceeds the melting point of Mg (the cooling part of the temperature profile also indicates solidification at 650 °C). Such a relatively

low temperature explains why no light emission is seen in the high-speed video images shown in Fig. 2.3.

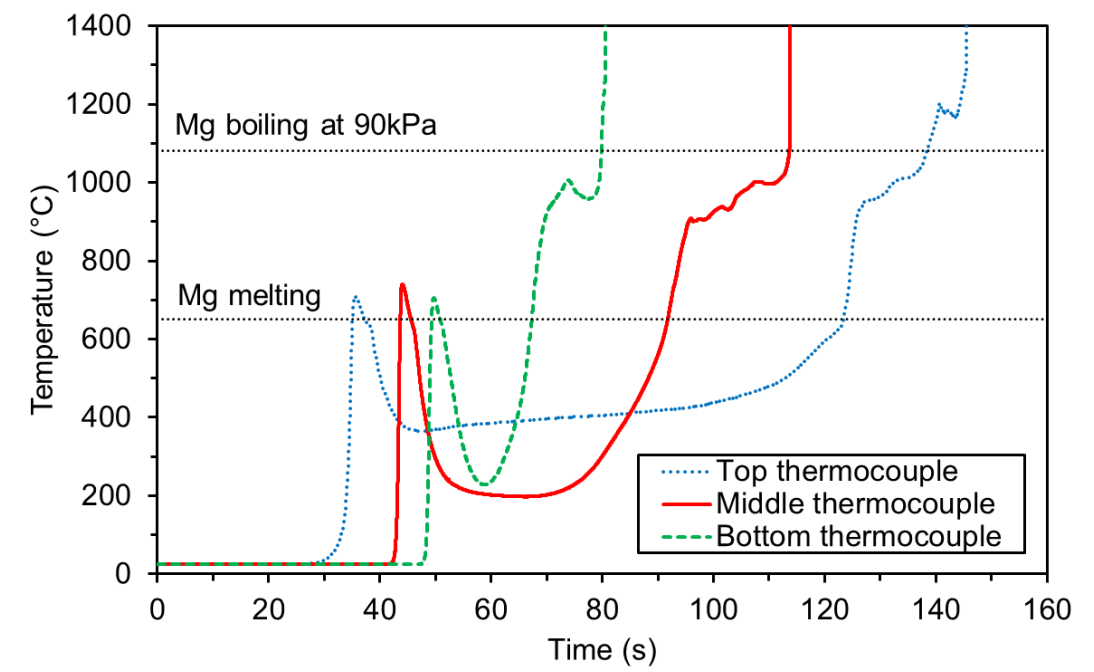

Figure 2.5: Temperature profiles measured by three thermocouples during combustion of Mg powder in oxygen at 90 kPa. Time zero corresponds to the laser pulse.

There are three possible sources of heat for the thermal wave that propagates downward: the laser pulse, the combustion of the top layer of the powder, and the oxidation of the powder in that wave. The energy delivered by the 125 ms laser pulse is 4 J, and only part of this energy is adsorbed by the powder. According to the mass measurements and estimates, the energy released by the top layer of the powder is of the order of 1 kJ, i.e., three orders of magnitude higher than that of the laser pulse, while the energy consumed by heating and melting the Mg particles is 0.7 – 0.8 kJ. To examine the particles after the propagation of the thermal wave downward, in one experiment at 90 kPa the oxygen environment was quickly replaced with argon right after the ignition started at the bottom. Figure 2.6 shows the SEM images of the quenched particles. It is seen that they are similar to the initial Mg particles shown in Fig. 2.1, which implies that only a

thin surface layer of the particle was oxidized. The oxide layer apparently maintained the shape of the particles during melting and prevented their sintering. Indeed, the sintering of Mg powders in oxygen-containing environments is known to be unfeasible because a thin stable oxide layer of 3–5 nm on the particle surface strongly inhibits sintering [39]. However, the oxidation of even a small amount of Mg could release a significant amount of heat, which contributed to the propagation of the thermal wave. The approximate constancy of the maximum temperature and acceleration of the front (as seen in the temperature profiles in Fig. 2.5) indicate that the counterflow combustion at a rather low conversion may occur. This is not surprising as it is known that the counterflow combustion waves can propagate at incomplete conversion [19-21, 28].

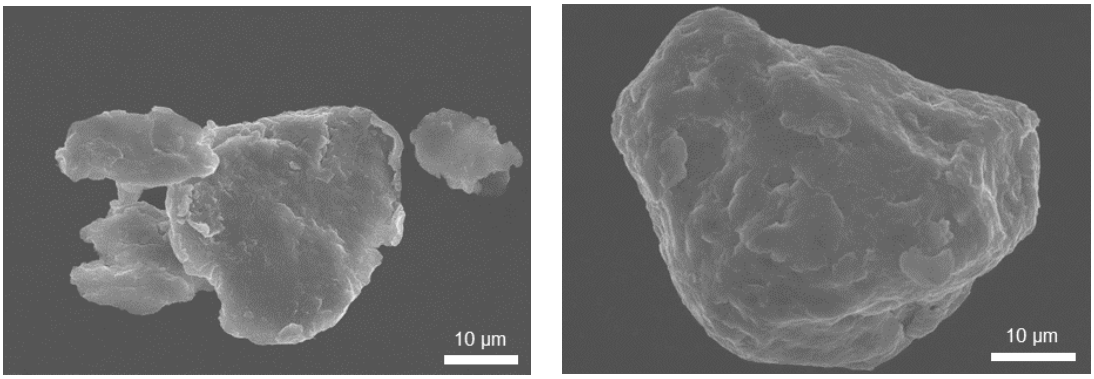

Figure 2.6: SEM images of Mg particles quenched after the first thermal wave.

In contrast, the maximum temperatures in the second wave exceeded the boiling point of Mg (1080 °C at 90 kPa) and destroyed the K-type thermocouples (the melting points of Chromel and Alumel are 1420 and 1399 °C, respectively). We have calculated the adiabatic flame temperature of an Mg/O_2 mixture at 90 kPa, using THERMO (version 4.3) software, which is based on the Gibbs free energy minimization and contains a database of approximately 3000 compounds [40]. The Mg/O_2 mole ratio in the initial mixture corresponded to the extent of conversion, 0.61, observed in this experiment. The obtained adiabatic flame temperature is as high as 3044 °C. Because of heat losses, the actual maximum temperatures were way below the melting

point of MgO, 2852 °C, since no melting or sintering of the products was observed, but still above the upper limit for the K-type thermocouples. It should be noted that during the coflow combustion, the infiltration of the gas through the hot products increases the temperature in the reaction zone, which may partly compensate for the cooling due to heat losses through the lateral surface.

The scanning electron microscopy of the combustion products provides additional evidence of Mg boiling and vapor-phase combustion. Figure 2.7 shows a typical SEM image, where it is seen that most particles are 1 – 2 μm in size. The particles have an irregular shape, often with flat surfaces and sharp edges. A prior SEM study of the combustion products of Mg/pyroxylin mixtures, where vapor-phase combustion of spherical Mg particles (mean volume diameter: 2, 11.6, and 76 μm) took place, showed that most product particles were cubes slightly smaller than 1 μm [41,42]. The particles formed in the present work look similar, which indicates that they formed via homogeneous condensation of MgO, produced by the gas-phase reaction of Mg vapor with oxygen.

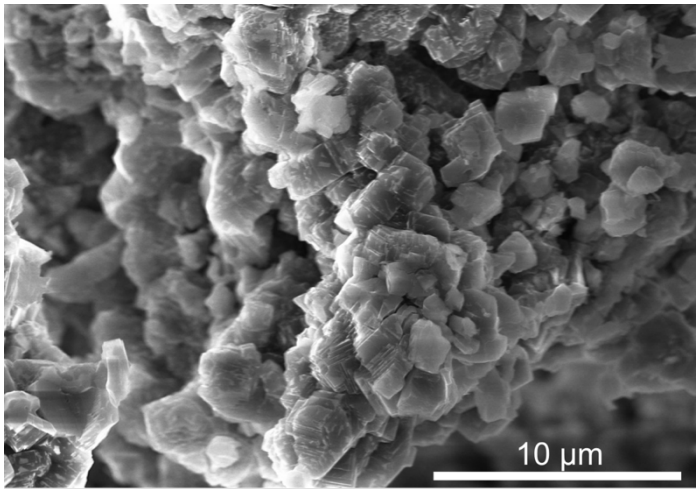

Figure 2.7: SEM image of the combustion products.

The experiments at pressures of 67, 53, and 44 kPa have shown the same behavior: two thermal waves. At 67 and 53 kPa, the second wave propagated upward over the entire sample.

However, in the experiments at 44 kPa the upward propagation of the combustion wave stopped after a short distance.

The upward propagation of the second wave is possible owing to the infiltration of oxygen from the bottom end through the formed MgO products, i.e., the coflow combustion occurs. While the porosity of the tested Mg powder was insufficient for effective infiltration of oxygen and counterflow propagation of the combustion front at a high conversion, the lower volume of MgO resulted in a greater porosity of the products (theoretically 77% at full oxidation of a powder with a porosity of 71% and Pilling-Bedworth ratio of 0.81). This increase in porosity enabled the coflow propagation.

To determine the axial velocity of the combustion front propagation, the video record of combustion in each experiment was thoroughly analyzed using the Phantom Camera Control application, which uses image filtering algorithms to smooth, emphasize, enhance, or isolate certain aspects of the images. Specifically, we used the Edge Hipass 5-by-5-pixel transition filter, which enhances in a high-frequency detail the edges of a figure in the images, such as the boundary between the combustion front and the unburned powder. Figure 2.8 shows the original and filtered images at four points of the propagation process at a pressure of 67 kPa. The initial, unsteady stage of the propagation (first 10 s in Fig. 2.8) is followed by a relatively steady propagation (next 72 s in Fig. 2.8). The average axial velocity of the combustion front was determined based on the length of steady propagation, i.e., the initial part of the process was not taken into account. To convert the pixels of the image to the distance, the axial velocity of the front u was calculated using the formula:

$$u = \frac{\Delta Y}{\Delta X}\frac{D}{t} \tag{2.3}$$

where ΔY is the distance traveled upward by the front based on the pixels coordinates, ΔX is the outer diameter based on the pixels coordinates, D is the outer diameter of the tube, and t is the time.

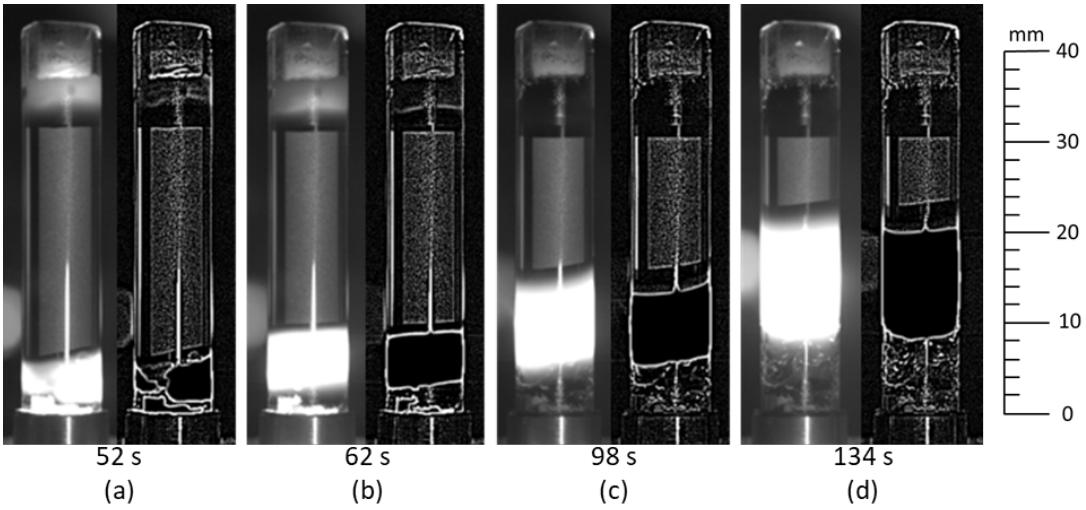

Figure 2.8: Original and filtered images of the combustion wave propagation. Time is relative to the laser pulse.

Figure 2.9 shows the extent of conversion vs. the average axial velocity of the combustion front in the experiments at 53, 67, and 90 kPa. Six tests without thermocouples were conducted at each pressure. The data obtained in seven tests with thermocouples, conducted at 90 kPa, were not taken into account because, as mentioned above, oxygen could penetrate into the powder in the places where the thermocouple wires were inserted, and heat losses to the thermocouple wires and the ceramic insulators could also increase the experimental uncertainty. It should be noted that the plot shows large variations of the combustion front velocity in the experiments conducted under the same conditions. Possible causes are discussed later in the paper.

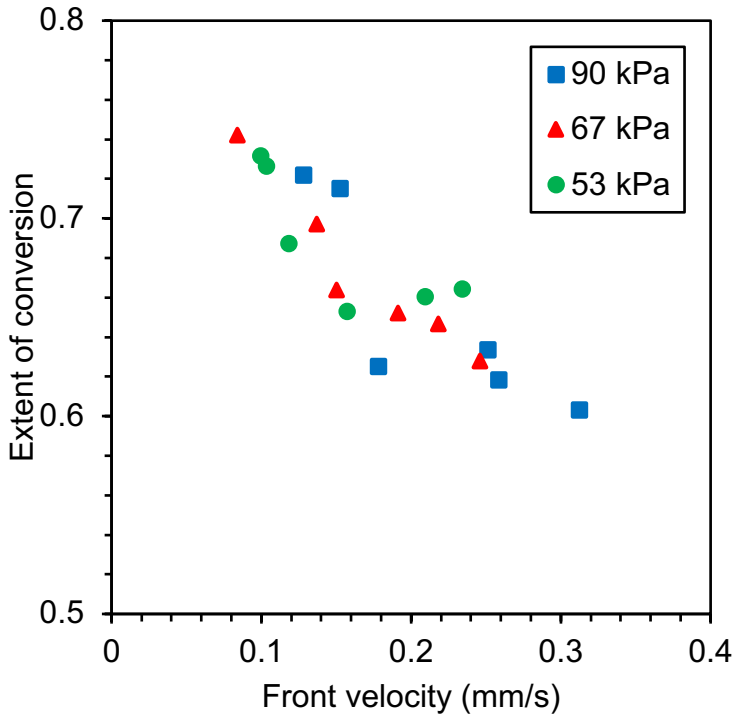

Figure 2.9: The extent of conversion vs. the average axial velocity of the front during combustion of Mg powder at 53, 67, and 90 kPa.

No clear effect of pressure is observed in Fig. 2.9. However, it is seen that a higher velocity of the front resulted in a lower extent of conversion. This is apparently associated with the fact that the propagation of the combustion front is controlled by two factors: conductive heat transfer from the front to the reactants and the infiltration of oxygen from the bottom end of the tube to the front. Interestingly, the modeling of counterflow combustion has also shown that the propagation at incomplete conversion leads to the inverse relationship between the front velocity and the extent of conversion: an increase in heat losses decreases the front velocity but increases the extent of conversion [21]. However, the author predicted full conversion during coflow combustion [21]. Apparently, in the present experiments, heat losses through the lateral surface and cooling of the formed MgO by the infiltrating oxygen play an important role. Driven by the thermal conduction, the front moves forward at an incomplete conversion if the oxygen infiltration is not sufficiently

rapid to fully oxidize the particles in the reaction zone. Without heat losses, the reaction zone would continue down to the bottom end, and all the metal would eventually be oxidized. In reality, the temperature decreases with increasing the distance from the front edge of the wave, and at a certain distance, the reaction becomes too slow.

It should be noted that the two-dimensional modeling of the combustion with infiltration of the oxidizer and heat losses has simulated the backward combustion wave that forms after the initial counterflow combustion wave with incomplete conversion has reached the open end [43]. It was shown that in the backward wave, the conversion could be complete along the central axis of the sample but incomplete near the lateral surface, where the heat is removed. This result supports the explanation that the coflow combustion at incomplete conversion is possible because of heat losses.

To get an additional insight into the mechanism of the combustion wave propagation, the flame thickness, i.e., the thickness of the bright zone as shown in Fig. 2.8, was determined in the middle of the relatively steady propagation in each experiment. Figure 2.10 shows the obtained values at different average axial velocities of the front. It is seen that the flame thickness is proportional to the front velocity.

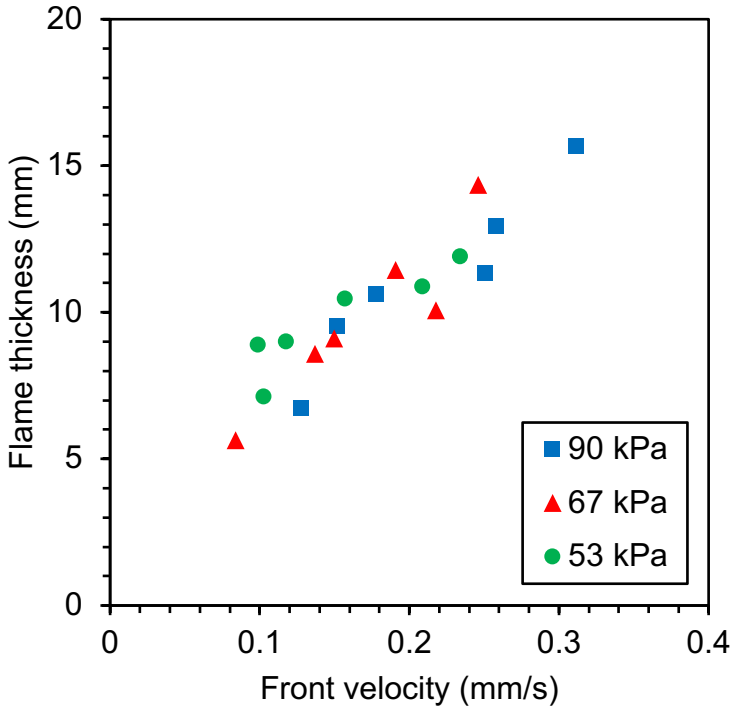

Figure 2.10: The flame thickness vs. the average axial velocity of the front during combustion of Mg powder at 53, 67, and 90 kPa.

It is difficult to quantify the observed rotation of the combustion wave. Often a single hot spot travels along a helical path, but sometimes two hot spots form, move in the opposite directions, and merge. Sometimes two hot spots propagate in the same direction. The transformation of one regime to another during the propagation was also observed. Yet, to obtain some quantitative information on the spinning propagation, the infrared video records from several experiments were analyzed with FLIR Altair software. Three experiments at 53 kPa with the lowest average axial velocities and three experiments at 90 kPa with the highest average axial velocities were taken for this analysis. In the images, 30 one-pixel points were selected along the vertical axis of the sample a constant distance apart. The software generated the temperature-time profile for each point. Figure 2.11 shows the temperature-time profiles obtained in one experiment at 53 kPa, where a successive propagation of two hot spots was observed (see Figure A2). The

initial part of the propagation at temperatures below 700 °C is not shown in this plot. It should be noted again that the temperatures were obtained at an emissivity of 1, so they are not actual temperatures. The five peaks correspond to five cases where the hot spot crossed the vertical line with the points. The number near each peak indicates the point where the temperature was the highest. It is seen that the first hot spot crossed the line in points 3, 12, and 21, while the second hot spot crossed it in points 17 and 27. Using the obtained data, the pitch, the axial velocity, and the tangential velocity were determined for each of the three rotation periods (the tangential velocity was determined for the outer diameter of the powder sample, i.e., the inner diameter of the quartz tube, 7 mm).

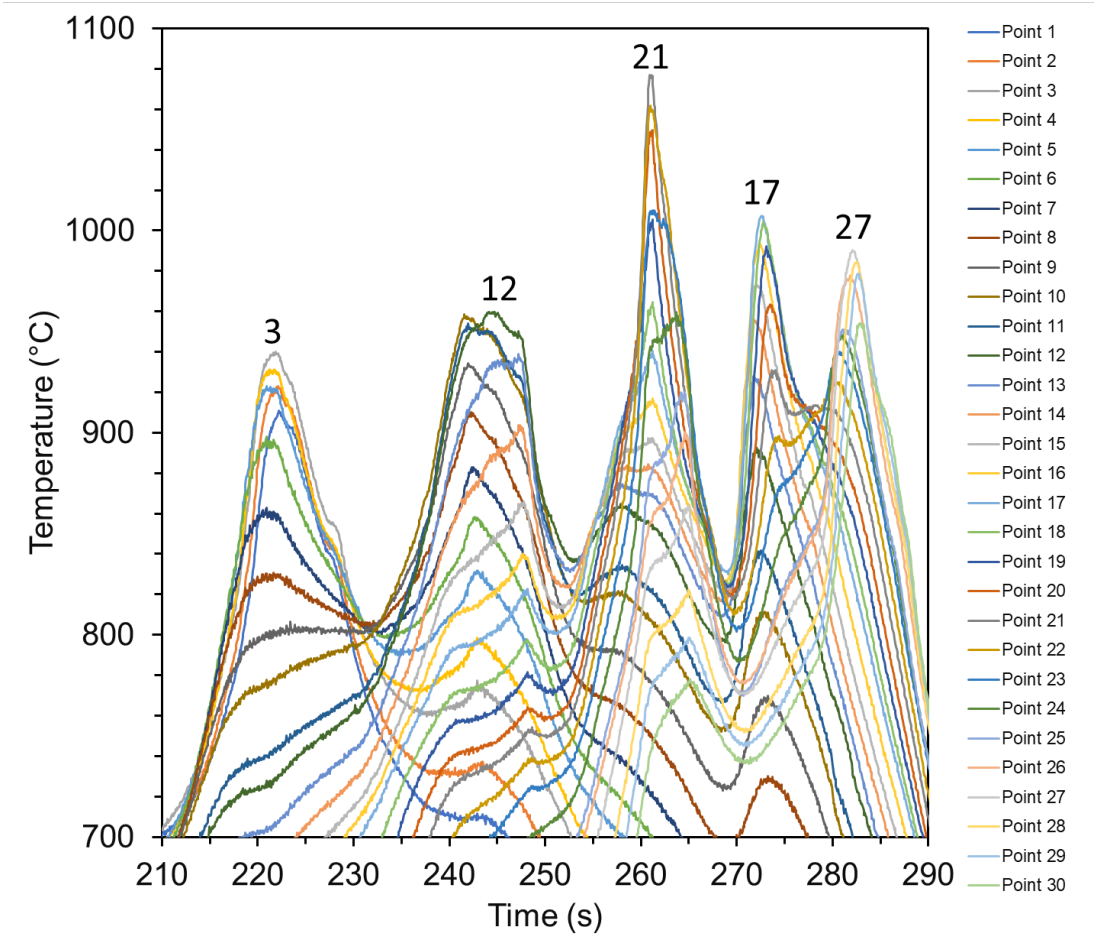

Figure 2.11: Temperature – time profiles in 30 points located along the vertical line 0.434 mm (seven pixels in the IR image) apart. Time relative to the laser pulse.

The analysis of the six selected experiments has revealed 14 rotation periods in total. The pitch was in the range of 2.7 – 6.5 mm, with no correlation to the axial velocity. Similarly, the frequency of rotations was in the range of 0.1 – 0.9 Hz, with no clear trend. Figure 2.12 shows the tangential velocity as a function of the axial velocity for the 14 rotation periods. It is seen that there is a linear relationship between these parameters, and the tangential velocity is approximately five times higher than the axial one. Note that the axial velocity here is local (related to a single rotation period), i.e., different from the average axial velocity shown in Figs. 2.9 and 2.10.

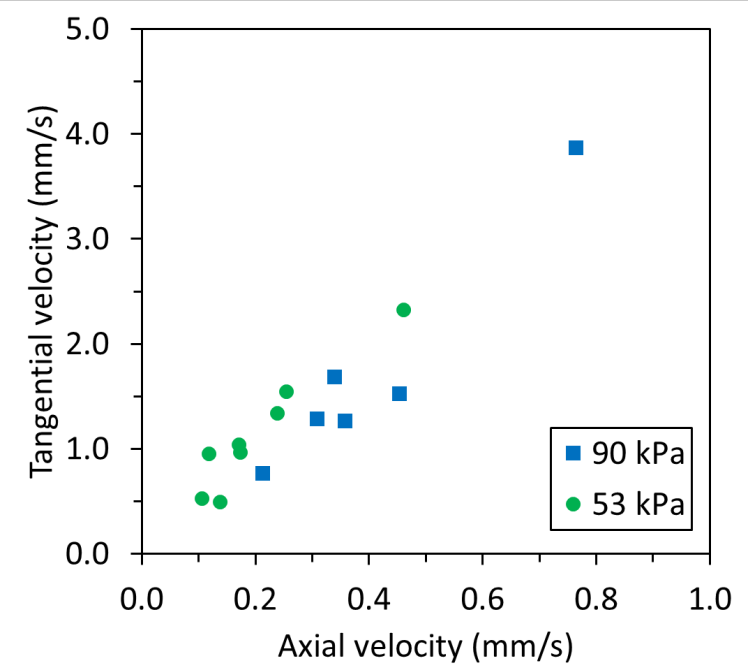

Figure 2.12: The tangential velocity vs. the axial velocity of the spinning propagation of the combustion wave at 90 kPa and 53 kPa.

The observed variations of the front velocity and the extent of conversion (see Fig. 2.9) may be associated with the variations of porosity. Indeed, a decrease in porosity increases thermal diffusivity, which accelerates the thermal wave. However, at the same time, it decreases the permeability, which decreases the oxygen flux and results in a lower extent of conversion. To verify that the observed effects were caused by the variations of porosity, we looked at potential

dependencies of the average axial velocity of the front, the average flame thickness, and the extent of conversion on the measured porosity. Table 2.1 shows these values. Unfortunately, this analysis has not resulted in clear dependencies, which may be related to experimental uncertainties such as a non-uniform porosity of the sample and fluctuations of the velocity and thickness of the front during the propagation. The analysis of the instant velocities indeed shows significant fluctuations. Further, the penetration of oxygen into the sample through the supporting structure at the bottom (see Section 2.2) could not be controlled, so the random variations of the permeability of that structure could affect the oxygen flow rate and hence the combustion characteristics. However, as noted in Section 2.2, in the experiments with the powder densified to about 60% porosity, only the top layer burned, and no self-sustained combustion was observed. Therefore, the decrease in porosity from 68-74% to 60% had a strong effect.

Table 2.1: The combustion characteristics and the porosities of powder samples.

Axial velocity mm/s	Flame thickness mm	Extent of conversion	Porosity %
	Pressure: 90 kPa		
0.128	6.7	0.72	68.9
0.152	9.5	0.72	71.4
0.178	10.6	0.63	73.6
0.251	11.3	0.63	70.4
0.258	12.9	0.62	69.8
0.312	15.7	0.60	70.7
	Pressure: 67 kPa		
0.084	5.6	0.74	68.3
0.137	8.6	0.70	71.3
0.150	9.1	0.66	70.1
0.191	11.5	0.65	71.2
0.218	10.1	0.65	70.8
0.246	14.3	0.63	71.9
	Pressure: 53 kPa		
0.099	8.9	0.73	72.4
0.103	7.1	0.73	72.1
0.118	9.0	0.69	71.7
0.157	10.5	0.65	71.1
0.209	10.9	0.66	71.9
0.234	11.9	0.66	70.2

It is remarkable that the axial velocity of the front in the conducted experiments was rather low, of the order of 0.1 mm/s. Such low velocities are rarely seen in combustion systems, but they are typical for chemical oxygen generators [29,44].

2.4 CONCLUSIONS

Combustion of a magnesium powder at natural infiltration of oxygen has been studied experimentally. The powder sample, placed in a vertical quartz tube, was ignited at the top by an infrared laser beam in oxygen environments at pressures of 44 – 90 kPa. After rapid combustion of the top layer, a thermal wave propagated downward, followed by ignition at the bottom and propagation of a second wave upward. The second wave propagated at an axial velocity of the order of 0.1 mm/s in the coflow combustion regime at incomplete conversion.

For the first time, an oscillatory instability of the flame front, specifically a spinning combustion wave, was observed for metal-gas systems where the gaseous oxidizer is a deficient component that infiltrates along the sample axis. The tangential velocity of the spinning propagation was approximately five times higher than the axial velocity.

The results demonstrate that if a metal with a low Pilling-Bedworth ratio is used, the coflow combustion regime is possible. The combustion characteristics are sensitive to the availability of the infiltrated oxygen. An increase in the axial velocity of the combustion wave is accompanied by an increase in the flame thickness and a decrease in the extent of conversion.

Chapter 3: Oxidation and Combustion of Stabilized Lithium Metal Powder (SLMP)

3.1 INTRODUCTION

In many future space missions, the use of solar or nuclear energy will be unfeasible or impractical. Thus, there is a need for power systems based on combustion, which potentially offer high specific energies and long storage times as compared to the best batteries. Recently, we have proposed to develop power systems where a metal powder burns with oxygen supplied by a chemical oxygen generator such as those used in aircraft, submarines, and space stations [45]. Since potential metal fuels burn with CO_2, in the missions to Venus and Mars the atmospheric CO_2 could be added to the oxygen flow, thus increasing the specific energy of the system.

Specifically, we propose to fill a cylindrical reactor with the metal powder and feed the oxygen into it. The ignition at one end will trigger the propagation of a self-sustaining combustion wave over the powder. Such a process, commonly called filtration combustion, has been used for self-propagating high-temperature synthesis (SHS) of various metallic and nonmetallic nitrides and hydrides [14,15]. Depending on the location of the ignition source relative to the oxidizer inlet, two propagation modes are possible in the filtration combustion. In the coflow mode, the oxidizing gas infiltrates through the combustion products, while during the counterflow combustion the gas infiltrates through the initial powder.

Prior experimental and modeling studies of the filtration combustion have been conducted primarily at so high pressures of the reacting gas that the density of the gas in the pores between the particles is comparable with that of the metal fuel. In the proposed combustors for space power systems, the gas pressure is relatively low, so the infiltration should be sufficiently rapid to provide enough gas for the reaction. The combustion under these conditions has been studied less.

Recently, we have investigated combustion of a magnesium (Mg) powder placed in a quartz tube inside a closed chamber filled with oxygen at pressures of 44–90 kPa [45]. The oxygen could infiltrate into the powder from both ends. The infiltration was caused by the consumption of oxygen and hence a decrease in pressure in the reaction zone ("natural" infiltration [14]). Laser ignition at the top resulted in the propagation of a counterflow combustion wave at low conversion followed by a second ignition near the bottom and the backward propagation of a coflow wave. This has demonstrated that if a metal with a low Pilling-Bedworth ratio (product/metal volume ratio, 0.81 for Mg) is used, coflow combustion is possible. For comparison, aluminum has a Pilling-Bedworth ratio of 1.28, so the produced alumina would prevent oxygen infiltration and coflow combustion.

Compared to Mg, lithium (Li) has a lower Pilling-Bedworth ratio and a higher specific energy: 0.57 vs 0.81 and 20 MJ/kg vs 15 MJ/kg, respectively (it is assumed here that Li is oxidized to Li_2O). Therefore, Li could be advantageous over Mg in this application. However, until recently, lithium powders were not commercially available. Currently, a stabilized lithium metal powder (SLMP®) is available from Livent, Inc. It consists of spherical particles coated with lithium carbonate (Li_2CO_3) to make the powder non-pyrophoric in a dry air environment [46]. Figure 3.1a shows a typical SEM image of an SLMP particle (diameter: 29 μm), while Figure 3.1b shows the protective coating detached from an electrochemically reacted particle. The contents of Li and Li_2CO_3 are 97 wt% minimum and 0.5 wt% minimum, respectively [47]. This powder has the potential to improve Li-ion batteries [46] and enable the development of Li-metal batteries [48,49].

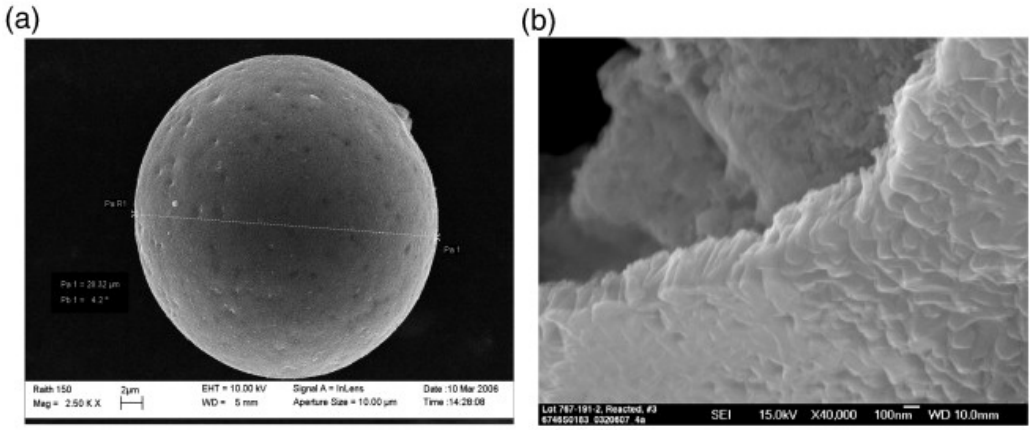

Figure 3.1: SEM images of (a) an SLMP particle and (b) a broken edge of the coating on a reacted SLMP particle [46].

To our knowledge, there is no information on the high-temperature oxidation and combustion of SLMP. The objective of the present work was to fill this gap and study oxidation of SLMP in O_2 and CO_2 environments using thermogravimetric analysis (TGA) and differential scanning calorimetry (DSC) at atmospheric and higher pressures as well as its combustion with O_2 and CO_2 at natural infiltration of the oxidizing gas. An additional application of the present work is fire safety during technological procedures that involve SLMP. The information on Li oxidation and combustion in CO_2 could also be of interest for the recently proposed concept of using lithium as a recyclable metal fuel for energy storage in solar and wind power plants [50,51].

3.2 EXPERIMENTAL

The SLMP was received in argon-filled containers from Livent, Inc. and used as is. According to the manufacturer, the tested powder lot contains 97.8 wt% atomic Li and 0.5 wt% Li_2CO_3; all particles are smaller than 129 μm, and the median diameter is 50 μm. Oxygen (99.994 % pure), argon (99.999% pure), and carbon dioxide (99.999% pure) were obtained from Airgas.

For the TGA tests, a small (0.5–0.9 mg) sample of the powder was uniformly spread over the bottom of an alumina crucible (diameter: 6 mm, volume: 85 μL) inside an argon-filled

glovebox. Next, the sample was transferred in a closed container to a thermogravimetric analyzer (Netzsch TG 209 F1 Iris) to be heated under a continuous gas flow (O_2/Ar or CO_2). Isothermal tests were performed at 300, 350, 400, and 450 °C. In non-isothermal tests, the sample was heated at 1, 2.5, 5, and 10 K/min. The thermocouple, attached to the holder of the crucible, was calibrated for each heating rate by using the melting points of four metal standards (In, Bi, Al, and Ag) and the c-DTA® (Netzsch) technique.

To obtain more information on the reactions of SLMP with CO_2, differential scanning calorimetry (DSC) was used. The samples (0.5–0.7 mg), prepared using the same procedure as for the TGA tests, were heated in a calibrated differential scanning calorimeter (Netzsch DSC 404 F1 Pegasus) at rates of 2.5 and 10 K/min in CO_2 flow for atmospheric pressures and in a high-pressure DSC (Netzsch DSC 204 HP Phoenix) at 10, 30 and 50 bar with a heating rate of 10 K/min in a CO_2 environment.

The combustion experiments were conducted in a laser ignition setup, previously used for experiments with reactive mixtures [29-32] and recently in the study on filtration combustion of Mg [45]. The setup includes a stainless-steel vacuum chamber (11.35 L) connected to a vacuum pump and a compressed gas cylinder. It is equipped with two window-door ports and two windows. The absolute pressure in the chamber is measured by a Pirani capacitance diaphragm vacuum gauge (Inficon PCG554).

The ignition system includes a CO_2 laser (Synrad Firestar ti-60), an infrared beam of which (wavelength: 10.55–10.68 μm, diameter: 2.0 ± 0.3 mm) enters the chamber vertically through a zinc selenide window in the lid. The power of the beam was measured with a powermeter (Synrad PW-250) and controlled by a laser controller (Synrad UC-2000), while the duration of the laser pulse was set using LabVIEW (National Instruments) software connected to the laser controller.

In the experiments reported in the present paper, the power of the beam after passing the zinc selenide window was 32 W, while the laser pulse duration was typically 0.25 s (in some tests where ignition did not occur, a duration of 0.5 s was used).

Quartz tubes (length: 40 mm) were used to hold the metal powder during the experiment. The tube was installed vertically in a stainless-steel holder, several alumina tubes (length: 10 mm, outer diameter: 1.0 and 1.6 mm) were installed vertically at the bottom of the quartz tube, and a thin layer of thermal insulation paper (Fiberfrax) was placed on top of the alumina tubes to support the metal powder (Fig. 3.2). The alumina tubes were used to locate the bottom of the powder sample above the top of the steel holder so that the whole sample could be seen.

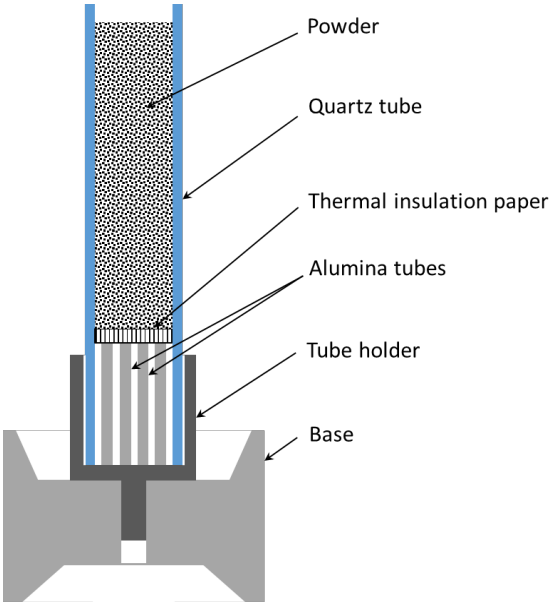

Figure 3.2: Schematic of the sample installation.

The quartz tube was filled with the tested powder in an argon-filled glovebox. The holder with the tube was then transferred to the setup in a closed container and installed on a brass pedestal inside the chamber. The infrared beam of the CO_2 laser was aligned with the center of the top end of the sample using a red beam of a laser diode pointer (Synrad), pre-aligned with the infrared beam. The combustion process was recorded at 250 fps with a high-speed video camera (Vision

Research Phantom v1210), equipped with a lens for macro shooting (Nikon AF Micro NIKKOR 60 mm f/2.8D).

The condensed products of oxidation and combustion were examined with scanning electron microscopy (Phenom ProX G6 Desktop SEM). X-ray diffraction analysis (Bruker D8 Discover XRD) of the products formed during the TGA and High-pressure DSC in CO_2 flow was also conducted.

3.3 RESULTS AND DISCUSSION

3.3.1 Oxidation of Li in an O_2/Ar environment

In the TGA tests on the oxidation of SLMP particles by oxygen, the samples were heated in a 60 mL/min O_2/Ar (10% O_2) gas flow.

Figure 3.3 shows the thermogravimetric curves obtained at heating rates from 1 to 10 K/min. The total mass gain is close to the value for full conversion of Li to Li_2O (115%). The curves are not smooth; there is a distinct transition from the first stage to a faster second stage.

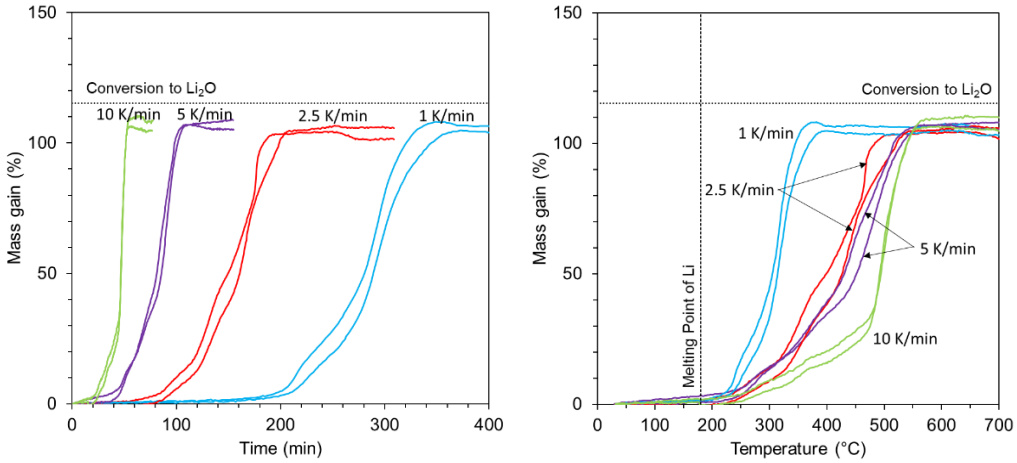

Figure 3.3: TGA of Li oxidation in O_2/Ar flow at heating rates of 1 – 10 K/min.

Figure 3.4 shows the SEM images of oxidized SLMP particles from a non-isothermal TGA test (heating rate: 1 K/min). It is seen that the particles are hollow spheres. In many of them, a hole in the shell is clearly seen. The formation of hollow shells is explained by the fact that the oxidation rate becomes significant only after melting of Li (180.5 °C), while the shell consists of solid products. Apparently, during the oxidation the molten lithium spreads outward through the pores in the shell and reacts with oxygen at the outer surface. Simultaneously, a cavity forms and grows inside the droplet. What caused the rupture of the shell remains unknown.

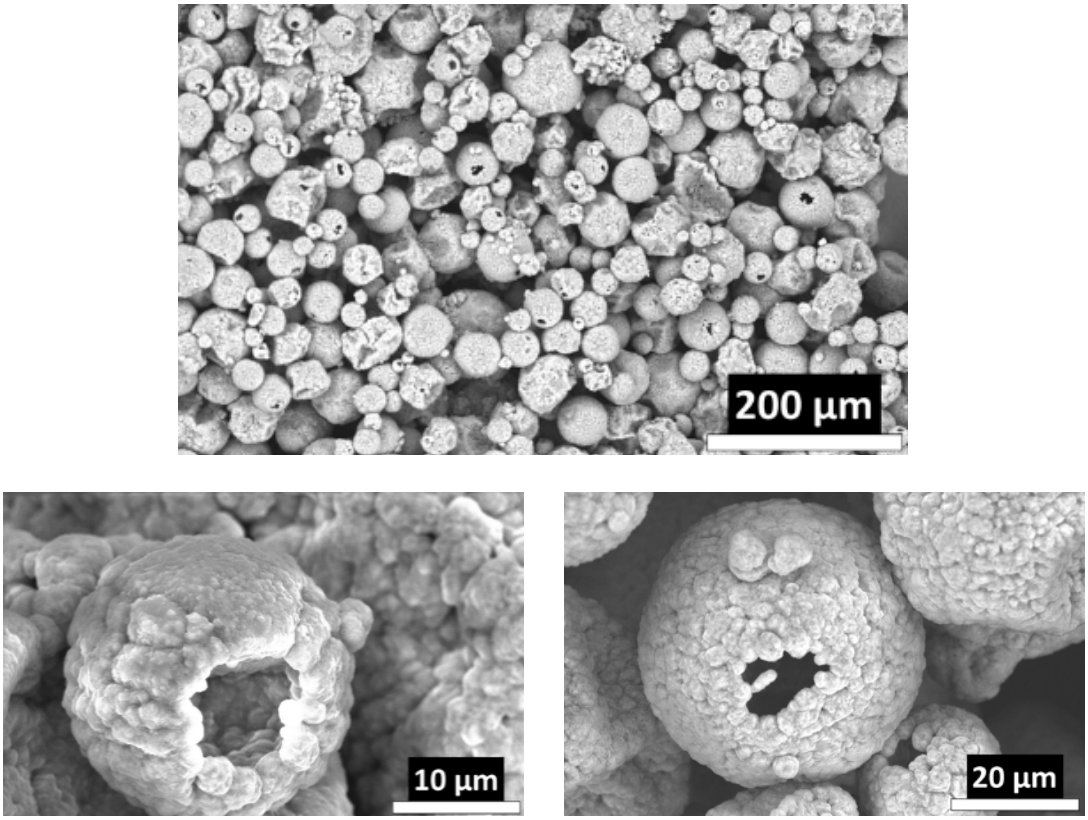

Figure 3.4: SEM images of oxidized Li particles.

Figure 3.5 shows the TGA curves from isothermal oxidation tests at temperatures varying from 300 to 450 °C. The mass gain during the initial temperature ramp (50 K/min) was negligible. Unexpectedly, the mass gain in the tests at 300 and 350 °C exceeded the value for conversion to

Li_2O. This indicates that at these temperatures lithium peroxide (Li_2O_2) formed along with Li_2O (the mass gain for conversion of Li to Li_2O_2 is 231%). In the isothermal tests at 400 and 450 °C, only Li_2O forms because Li_2O_2 decomposes within the temperature range of 300–400 °C [52-54].

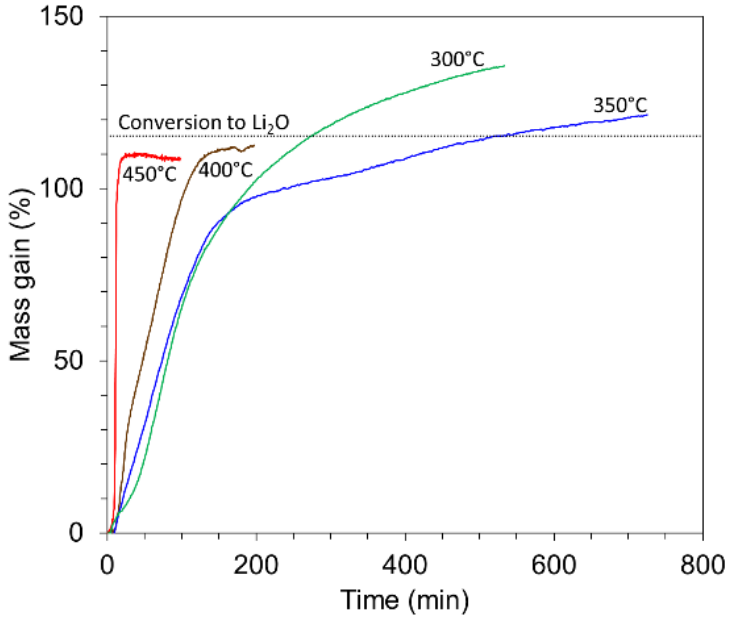

Figure 3.5: TGA of Li oxidation in O_2/Ar flow at temperatures 300 – 450 °C.

To verify the formation of Li_2O_2, a test was conducted where after 600 min of heating at 300 °C the temperature was raised at a rate of 50 K/min up to 450 °C. As shown in Fig. 3.6, this resulted in the loss of mass down to the value that corresponds to full conversion to Li_2O, which is explained by the decomposition of Li_2O_2. The observed small difference from the full conversion can be partly related to the fact that the tested Li particles include the Li_2CO_3 coating.

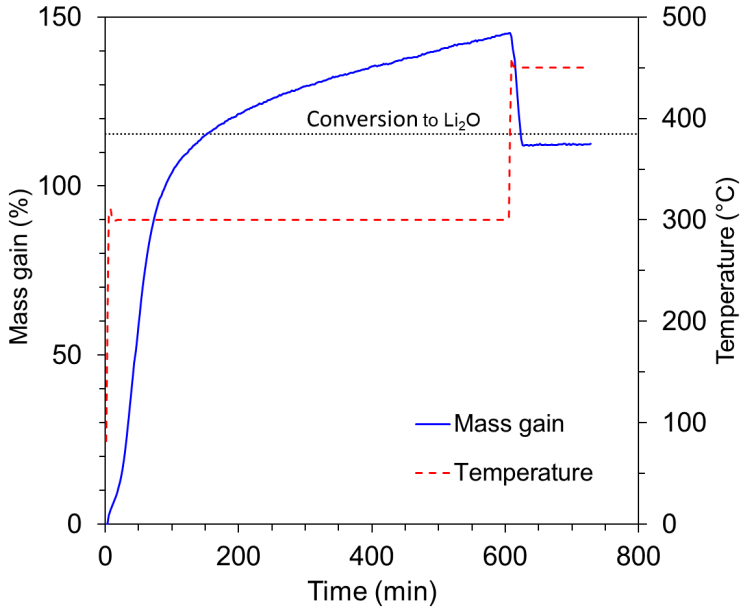

Figure 3.6: TGA of Li oxidation in O_2/Ar flow at 300 °C with a rise to 450 °C after 600 min.

During the non-isothermal tests, the decomposition of Li_2O_2, formed during the first stage of oxidation, accelerates the reaction because the product layer becomes more porous (the Pilling-Bedworth ratio is 76% for Li_2O_2 layer vs. 57% for Li_2O). This may explain the transition to a faster oxidation observed in the TGA curves shown in Fig. 3.3.

Figure 3.7a shows the SEM images of the particles after 600 min heating at 300 °C, while Figure 3.7b shows the particles that were then exposed to a temperature of 450 °C. It is seen that this temperature increase changed the microstructure. The shells in Fig. 3.7a have a multi-layer structure with cracks, while that in Fig. 3.7b consists of submicron grains, and the multi-layer structure is not clearly seen (the particle looks similar to those in Fig. 3.4). Apparently, this change in the microstructure is a result of Li_2O_2 decomposition.

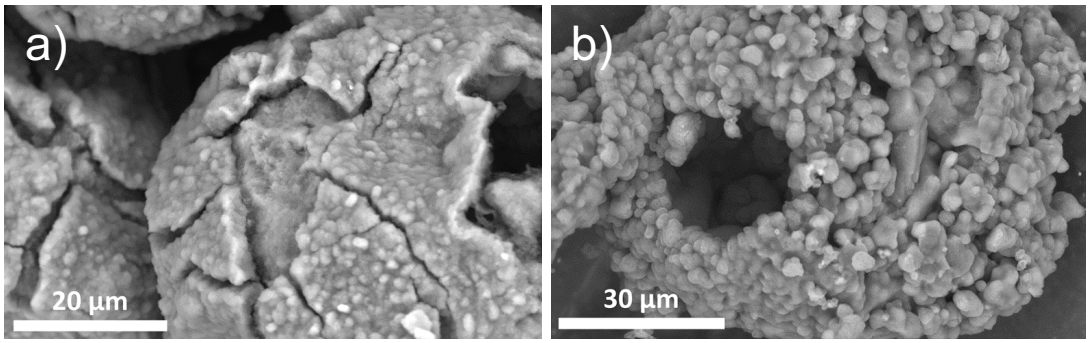

Figure 3.7: SEM images of Li particles after (a) isothermal oxidation at 300 °C and (b) isothermal oxidation at 300 °C followed by a temperature rise to 450 °C.

3.3.2 Combustion of Li at natural infiltration of O_2

The combustion experiments in oxygen were conducted at pressures 13–90 kPa. The inner diameter of the quartz tubes was varied from 2 to 7 mm (the wall thickness: 1 mm). Based on the measured mass and volume of each powder sample and the true particle density, the relative densities and the porosities were determined; the average values are 60.4 ± 4.7 and 39.6 ± 4.7, respectively.

In the tests with the smallest sample diameters (2 and 3 mm) at a pressure of 90 kPa, only the top layer burned. At sample diameters 4–7 mm and 90 kPa, a self-sustained propagation of the combustion wave was observed. For 7 mm samples, the combustion wave was observed over the entire range of pressures, and the combustion was so vigorous that the tubes were damaged (thermite reaction between Li and quartz apparently took place).

Figure 3.8 shows the images of a typical combustion process for a 4 mm sample. After the laser pulse, the top layer burns, emitting a lot of light (Fig. 3.8b). Simultaneously, the particles near the bottom move up, i.e., the powder is compressed, and a large gap forms near the bottom. Next, the combustion wave propagates downward (Figs. 3.8c–3.8d). After the combustion wave has reached the end of the now compressed sample (Fig. 3.8e), it continues to emit light for a

significant time. Next, the brightness decreases from both ends (Figs. 3.8f – 3.8g), and eventually all the sample becomes dark.

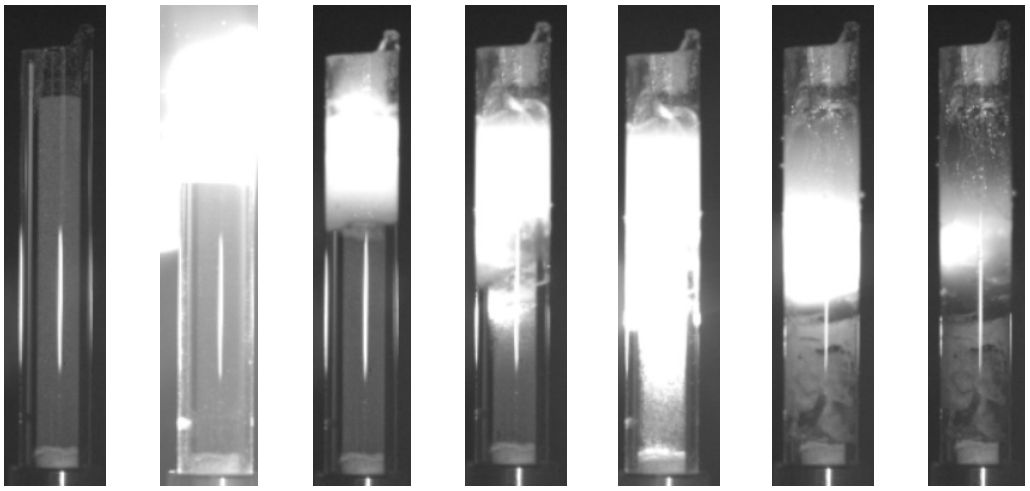

Figure 3.8: Combustion of Li powder (sample diameter: 4 mm) in oxygen at 90 kPa. Time is relative to the laser pulse.

Average velocities of the combustion wave, determined by the technique described in the paper on magnesium combustion [45], were in the range of 0.2–0.3 mm/s for tube diameters of 4–6 mm and pressure of 90 kPa. As noted in [45], such low velocities are rarely seen in combustion systems.

The extent of conversion was determined for each test based on the initial and final mass of the sample assuming that the product is Li_2O. The obtained values are 43±4%, 58±6%, and 63±10% for tube diameters of 4, 5, and 6 mm, respectively (based on five tests for each diameter at pressure of 90 kPa). It is worth mentioning that the propagation of the counterflow combustion wave at incomplete conversion was predicted in the theory of filtration combustion [19] and observed in the experiments on combustion of tantalum with nitrogen [28] and magnesium with oxygen [45].

In order to understand from what end the oxygen infiltrates during the combustion wave propagation, additional tests were conducted where the bottom end was closed with a 10 mm layer of a ceramic adhesive (Resbond 919, Cotronics). In these tests, the combustion of the top layer led to the motion of the particles and the formation of the gap near the bottom but not to the combustion wave. These results indicate that in the successful tests, the combustion wave propagated because oxygen infiltrated from the bottom. The motion of particles and formation of the gap near the bottom are explained by the reduced pressure in the sample due to the consumption of oxygen that was initially in the pores.

Apparently, the penetration of oxygen from the top was hindered by the formation of impermeable products. Indeed, Li_2O melts at 1438 °C, so the combustion of the top layer forms liquid lithium oxide, which prevents any oxygen penetration.

As noted in the Introduction, in the recent experiments with a magnesium powder, the counterflow combustion wave led to the ignition at the bottom followed by the propagation of the coflow combustion wave upward [45]. The temperature in the first wave was slightly higher than the melting point of Mg (650 °C), while the second wave involved vapor-phase combustion and much higher temperatures. The backward wave was possible because of the low extent of conversion in the first wave. In the experiments with SLMP, the counterflow combustion apparently generated very high temperatures, and the conversion was significant. In some experiments, a second wave did propagate upward (see Figure A3), but the first wave was still dominant.

3.3.3 Reactions of Li with CO_2

3.3.3.1 TGA and DSC at atmospheric pressure

In the TGA and DSC tests on the oxidation of SLMP particles by CO_2, the samples were heated in a 30 mL/min CO_2 gas flow at heating rates of 2.5 and 10 K/min up to 900 °C. Figure 3.9 shows the obtained TGA and DSC curves. It is seen that the reaction starts at the melting point of Li and sharply accelerates at approximately 400 °C. At about 135%, the mass gain stops but soon starts to increase again, eventually exceeding 400%. Once the temperature reaches the melting point of Li_2CO_3 (723 °C), the mass loss begins.

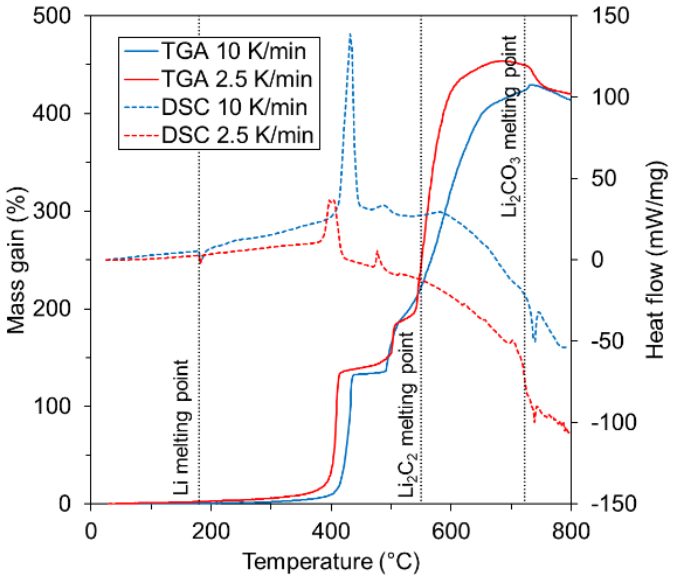

Figure 3.9: TGA and DSC of Li in CO_2 flow at heating rates of 2.5 and 10 K/min.

At the first stage of the reaction, lithium can react with CO_2 according to the equations:

$$2Li + CO_2 \rightarrow Li_2O + CO \quad (3.1)$$

$$4Li + CO_2 \rightarrow 2Li_2O + C \quad (3.2)$$

$$10Li + 2CO_2 \rightarrow 4Li_2O + Li_2C_2 \quad (3.3)$$

The absence of an endothermic peak at the melting point of Li_2C_2 in the DSC curves indicates that the reaction described by Eq. (3.3) does not occur. The mass gain would be 115% and 158% according to Eqs. (3.1) and (3.2), respectively. Therefore, the comparison with the experimental values (ca. 135%) indicates that the formation of carbon does occur though some amount of CO may also form.

Next, the formed lithium oxide starts to react with CO_2 producing Li_2CO_3. This is clearly seen in the XRD patterns of the products obtained by heating up to 500 and 600 °C (Fig. 3.10). The Li_2CO_3/Li_2O intensity ratio, determined for the highest peaks of the two phases, is equal to 0.2 at 500 °C and 3.0 at 600 °C. It should be noted that Li_2C_2 was not detected in the XRD pattern shown in Fig. 3.10a. The detection of lithium penta-aluminum oxide ($LiAl_5O_8$) in Fig. 3.10b indicates that some interaction with the alumina crucible took place.

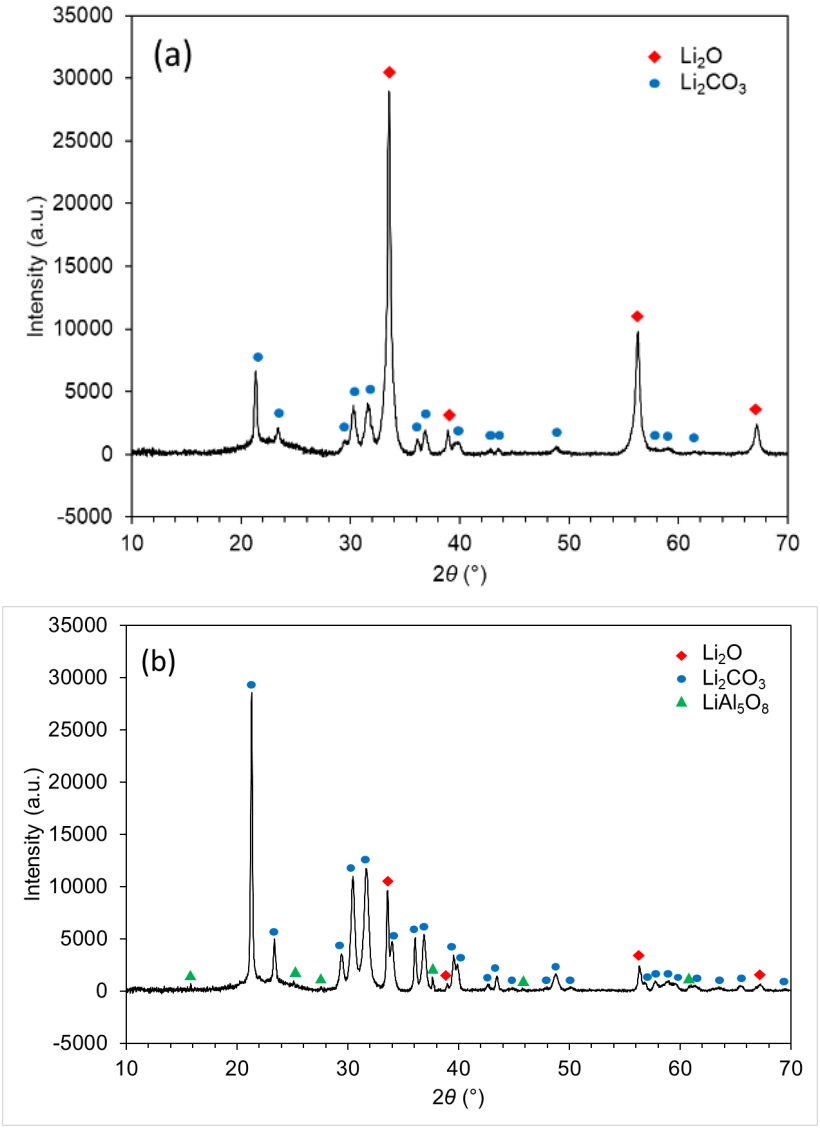

Figure 3.10: XRD patterns of products obtained during heating up to (a) 500 °C and (b) 600 °C.

In a recent study on the combustion of molten lithium with CO_2 in a batch reactor [4], it was suggested that the reaction of lithium oxide with CO_2 follows the equation:

$$Li_2O + CO_2 \rightarrow Li_2CO_3 \tag{3.4}$$

and the overall reaction of Li with CO_2 is:

$$4Li + 3CO_2 \rightarrow 2Li_2CO_3 + C \quad (3.5)$$

The mass gain in this reaction pathway is 476%. The experimental values of the maximum mass gain in the TGA data shown in Fig. 3.9 were 454% at a heating rate of 2.5 K/min and 429% at 10 K/min. The presence of the carbonate coating on the SLMP particles cannot explain such large deviations from the theoretical value. The lower mass gain may be caused by the reverse Boudouard reaction, which occurs at sufficiently high temperatures:

$$C + CO_2 \rightarrow 2CO \quad (3.6)$$

The overall reaction of Li with CO_2 in this case is:

$$2Li + 2CO_2 \rightarrow Li_2CO_3 + CO \quad (3.7)$$

and the resulting mass gain is 432%. Thus, in the experiment, the overall reaction apparently generates both C and CO.

The final loss of mass is explained by the decomposition of lithium carbonate, which starts after its melting [55,56].

Interestingly, the experiments with Li particles dropped into a vertical tube furnace have shown that their combustion in CO_2 includes a short vapor-phase burning stage, which produces Li_2O and CO, followed by a long surface-burning stage, which generates Li_2CO_3 [50]. The present TGA results also show first the formation of Li_2O and then its conversion into Li_2CO_3, but both stages involve surface reactions.

The Li-CO_2 combustion experiments were conducted at a pressure of 90 kPa. In contrast with the experiments in oxygen, a self-sustained propagation of the combustion wave over the Li powder was not achieved in a CO_2 environment. The reaction was observed only in the top layer of the sample (see Figure A4). This may be explained as follows. If the reaction described by Eq. (3.7) occurs, the produced CO will effectively prevent the infiltration of CO_2 through the pores between the particles. On the other hand, if the reaction described by Eq. (3.5) takes place, the condensed products form a barrier for the reaction (the product/metal volume ratio is 1.45). This was observed in the experiments with batch reactors [4], where the condensed products at the molten lithium surface terminated its reaction with CO_2, leading to a low combustion efficiency.

To investigate the reaction stages of Li in CO_2 at atmospheric pressure, we took SEM images of the samples quenched at different temperatures, specifically at 465 °C (after the 1st DSC peak at 2.5 K/min), at 525 °C (after the 2nd peak), at 695 °C (before the melting of Li_2CO_3) and at 800 °C (after the melting of Li_2CO_3), see Figure 3.9. The SEM images of these samples are shown in Figs. 3.11a, 3.11b, 3.11c, and 3.11d, respectively. The previously reported XRD data showed a significant increase in the Li_2CO_3/Li_2O ratio with increasing the temperature from 500 to 600 °C. In Fig. 3.11a, we observe the formed Li_2O grains. In Fig. 3.11b, the formed Li_2CO_3 layer has a smoother outer surface. In Fig. 3.11c, a spiky morphology is observed. Lastly, Fig. 3.11d shows the molten Li_2CO_3 along with whisker-like crystals, which apparently consist of Li_2O formed as a result of Li_2CO_3 decomposition.

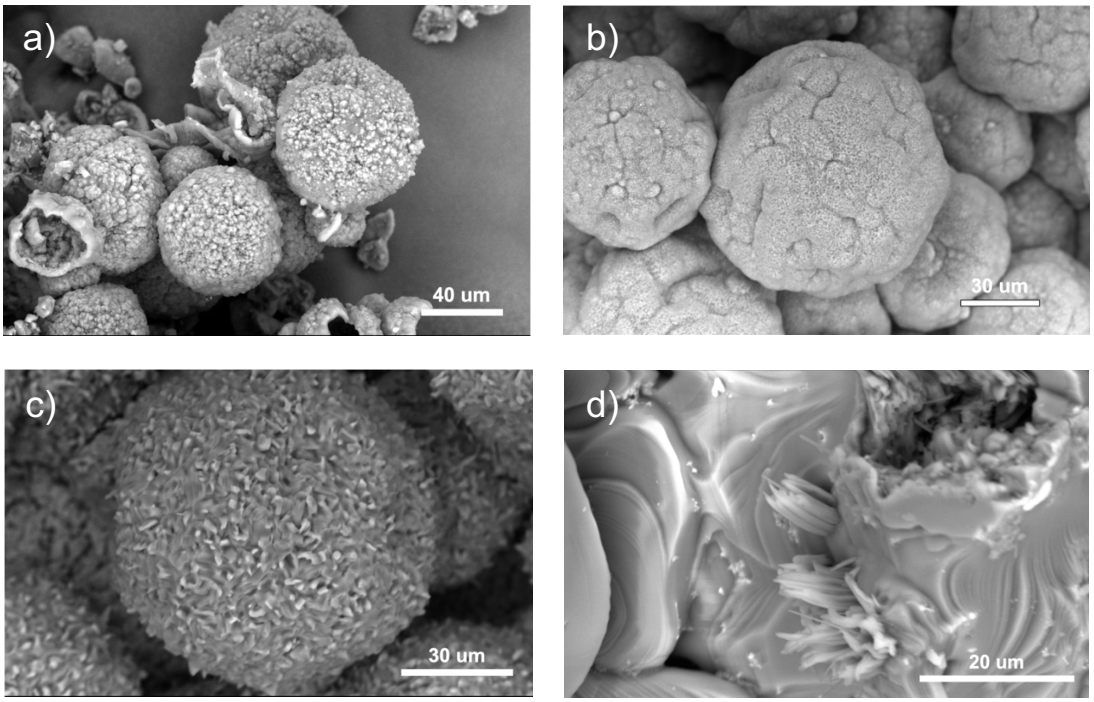

Figure 3.11: SEM images of samples quenched at (a) 465, (b) 525, (c) 695, and (d) 800 °C.

3.3.3.2 Detailed studies of the two stages of Li_2O-CO_2 reaction

It has been shown above that the 2nd stage of Li-CO_2 reaction is the reaction of the formed Li_2O with CO_2. To prove that all lithium powder was oxidized during the 1st stage of the reaction, heating and cooling DSC tests were conducted. In one test, lithium powder was heated up to 230 °C, i.e., 50 °C above the melting point of Li but two hundred degrees below the first stage of the reaction in CO_2. Figure 3.12 (top) shows the melting and solidification peaks in the DSC curve of Li powder. In a second test, lithium powder was heated up to 480 °C, i.e., after the first stage of the reaction but before the second stage. Figure 3.12 (bottom) shows no solidification peak in the cooling section of the DSC curve obtained in this test. This confirms full oxidation of Li during the first stage of the reaction.

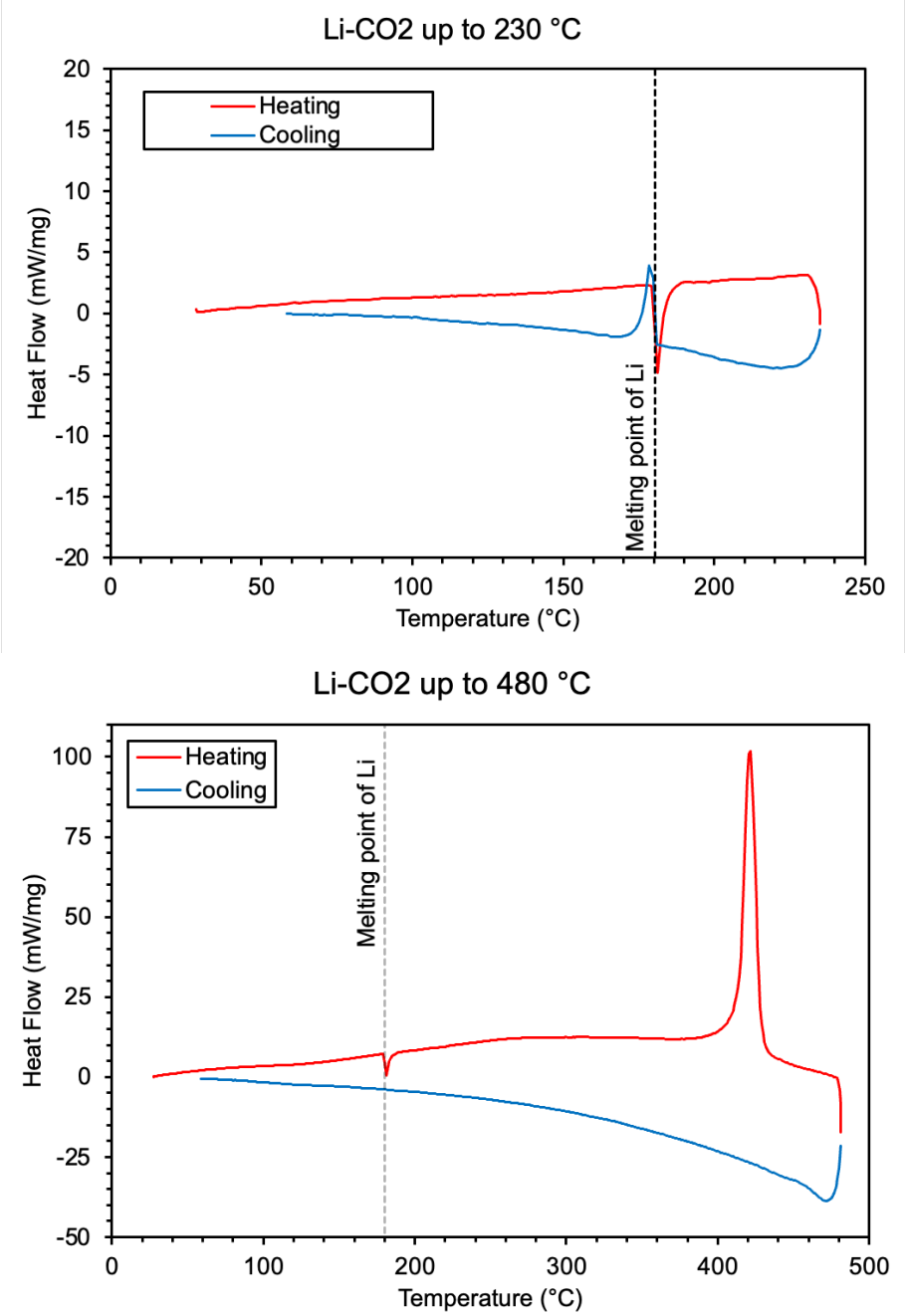

Figure 3.12: Heating (red) and cooling (blue) DSC tests of Li-CO_2 heated up to 230 °C (top) and 480 °C (bottom).

In order to confirm carbon formation during the 1st stage of Li-CO_2 (at about 400 °C), TGA tests were performed where the products formed in that stage were heated in O_2 flow. It was expected that carbon would be oxidized to form CO_2, which would be detected by mass measurements in the TGA. The Li powder was heated in CO_2 flow up to 460 °C. The sample was then cooled down to room temperature, and the system was evacuated to remove the remaining CO_2. Next, O_2 flow was established, and the products were heated up to 800 °C. Figure 3.13 shows the obtained TGA curve. It is seen that instead of decreasing, the mass increased close to 60%. Apparently, O_2 reacted with both C and Li_2O, producing Li_2CO_3.

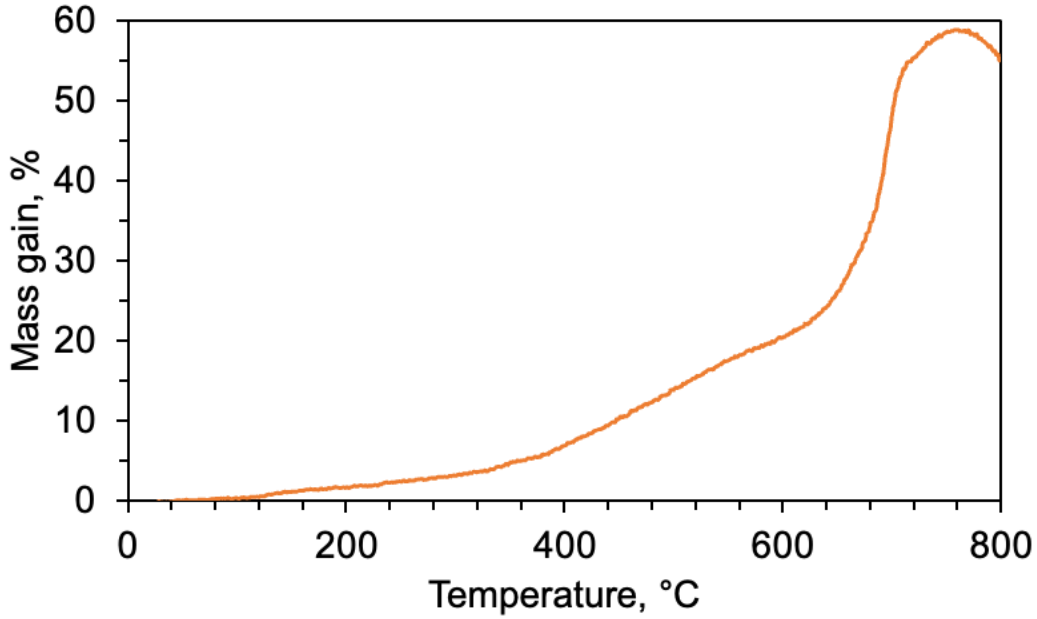

Figure 3.13: TGA of the products of the 1st stage of Li-CO_2 reaction heated in O_2 flow.

As all Li powder reacts during the 1st stage, the simulation of the 2nd stage was performed with TGA and DSC. The Li powder was initially oxidized in O_2 before being exposed to CO_2. Figure 3.14 shows the TGA and DSC curves of the obtained Li_2O heated up to 800 °C in CO_2 flow at a heating rate of 5 and 10 K/min. TGA data is similar to the data obtained for the reaction of Li_2O with CO_2 in [56]. A slow reaction starts at about 200 °C and accelerates after 500 °C. Both

TGA and DSC have shown that the fastest reaction was at 707 °C, which correlates with the peak in the DSC curve of Li in CO_2 at a heating rate of 2.5 K/min (see Figure 3.9).

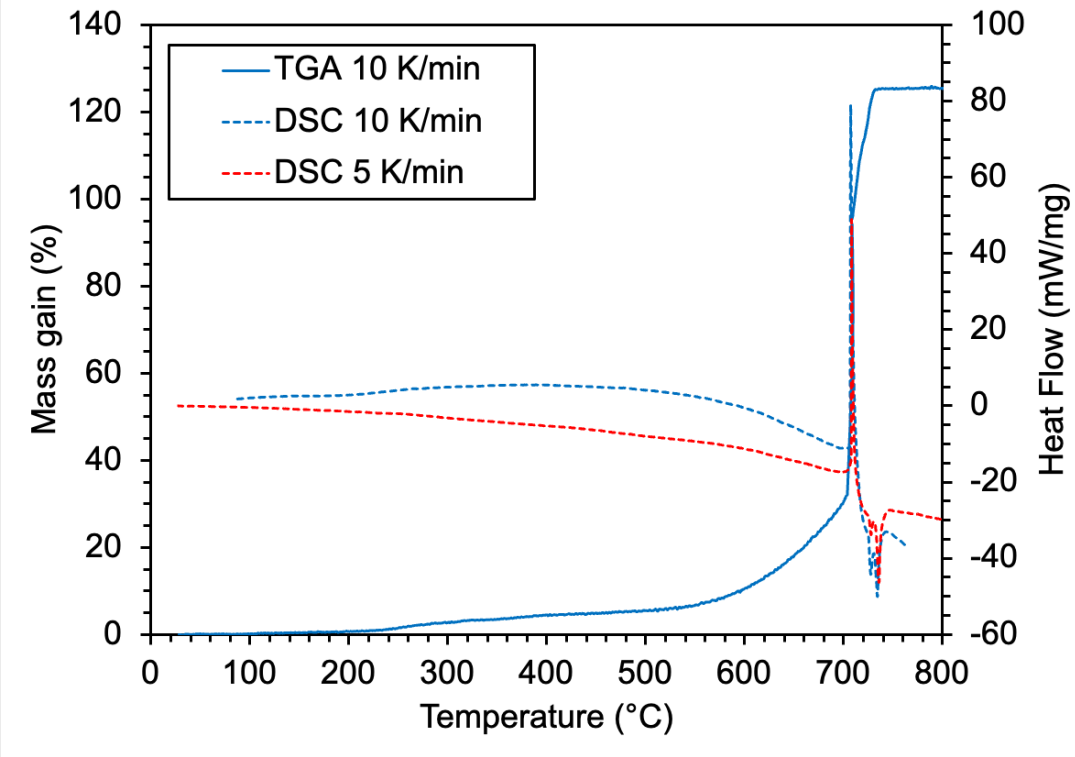

Figure 3.14: TGA and DSC of Li_2O-CO_2 reaction at a rate of 5 and 10 K/min

3.3.3.3 Li-CO_2 reactions at high pressures

The pressure in the CO_2 tank is equal to the saturated vapor pressure of CO_2, which is about 60 bar at room temperature. This limits the pressure in high-pressure DSC tests. For this reason, they were conducted at gauge pressures of 10, 30, and 50 bar (the atmospheric pressure was approximately 0.9 bar). The samples were heated at a heating rate of 10 K/min up to 600 °C, which is the maximum temperature allowed by the used instrument. Figure 3.15 shows the DSC curves obtained at gauge pressures of 0, 10, 30 and 50 bar. In this figure, the curve at 0 bar represents the 10 K/min DSC curve at atmospheric pressure shown in Figure 3.9. The temperature of the peak ranges from 431 °C to 443 °C, which is comparable to the previously measured temperature of the DSC peak at atmospheric pressure (431 °C at 10 K/min).

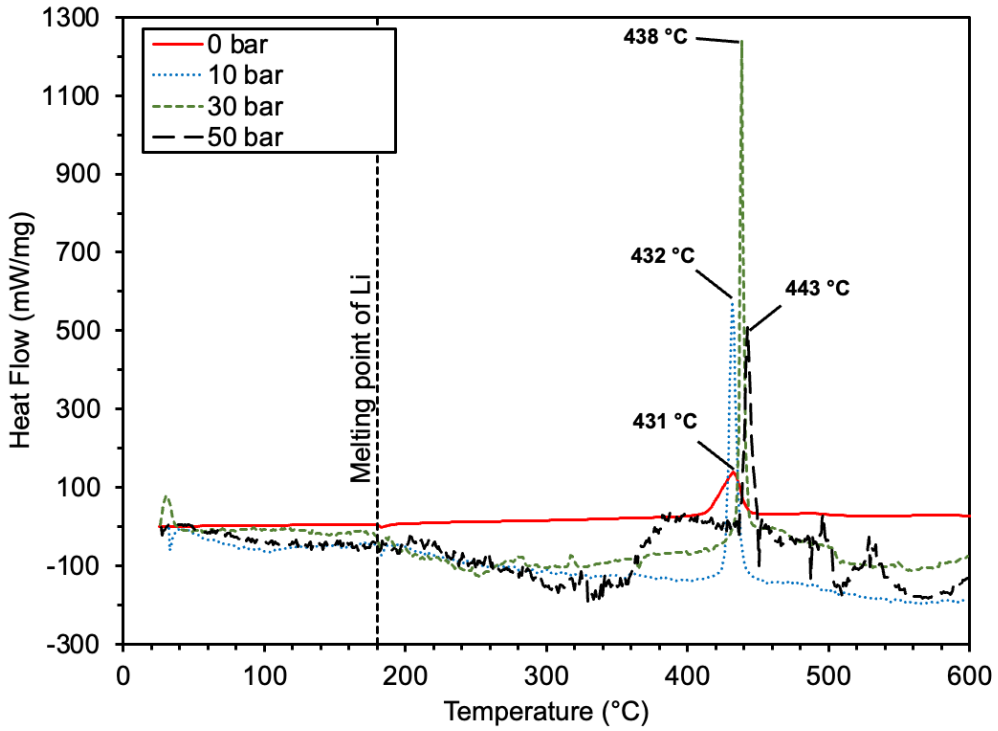

Figure 3.15: DSC curves of the Li-CO_2 reaction at gauge pressures of 0, 10, 30 and 50 bar.

Figure 3.16 shows additional tests at 10 and 30 bar with peak temperature ranging from 426 to 450 °C. Note that the peak at 50 bar in Fig. 3.15 is within this range. The results indicate that there is no apparent effect of pressure on the DSC peak temperature.

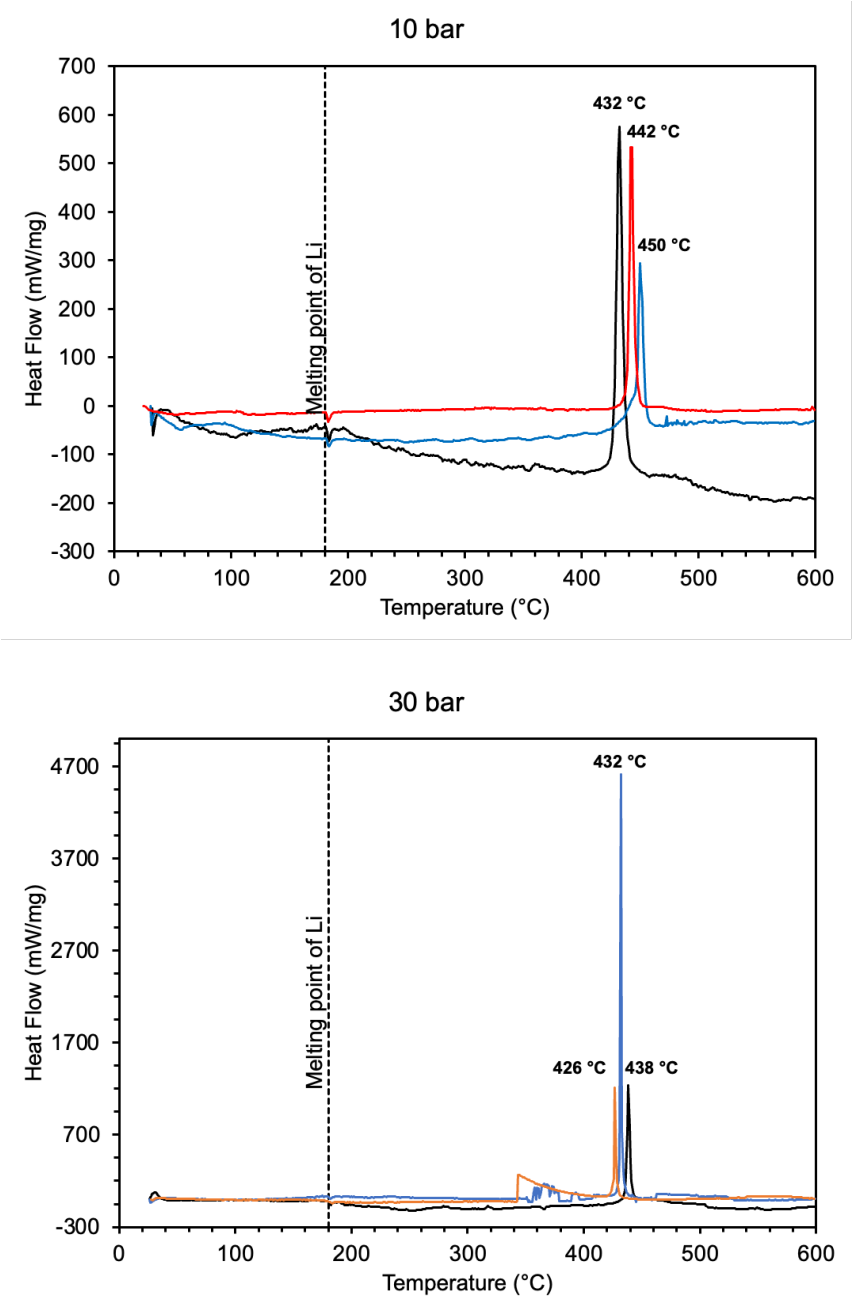

Figure 3.16: DSC curves of the Li-CO_2 reaction at gauge pressures of 10 and 30 bar.

The condensed products were examined with XRD analysis. Figure 3.17 shows the XRD patterns of the products obtained at 10 bar and 30 bar. It is seen that at 10 bar, both Li_2O and Li_2CO_3 are present, like in the tests at atmospheric pressure (see Figure 3.10). However, at 30 bar Li_2CO_3 is the only product. Note that the maximum temperature was 600 °C, while in the TGA at atmospheric pressure, a temperature of about 700 °C was required for the full conversion into Li_2CO_3 (see Fig. 3.9). The XRD pattern of the products obtained at 50 bar has also shown that Li_2CO_3 is the dominant phase. Although two peaks were not identified, there is no lithium oxide in the pattern. Therefore, the increase in pressure to 30 or 50 bar has promoted the conversion of the sample into Li_2CO_3.

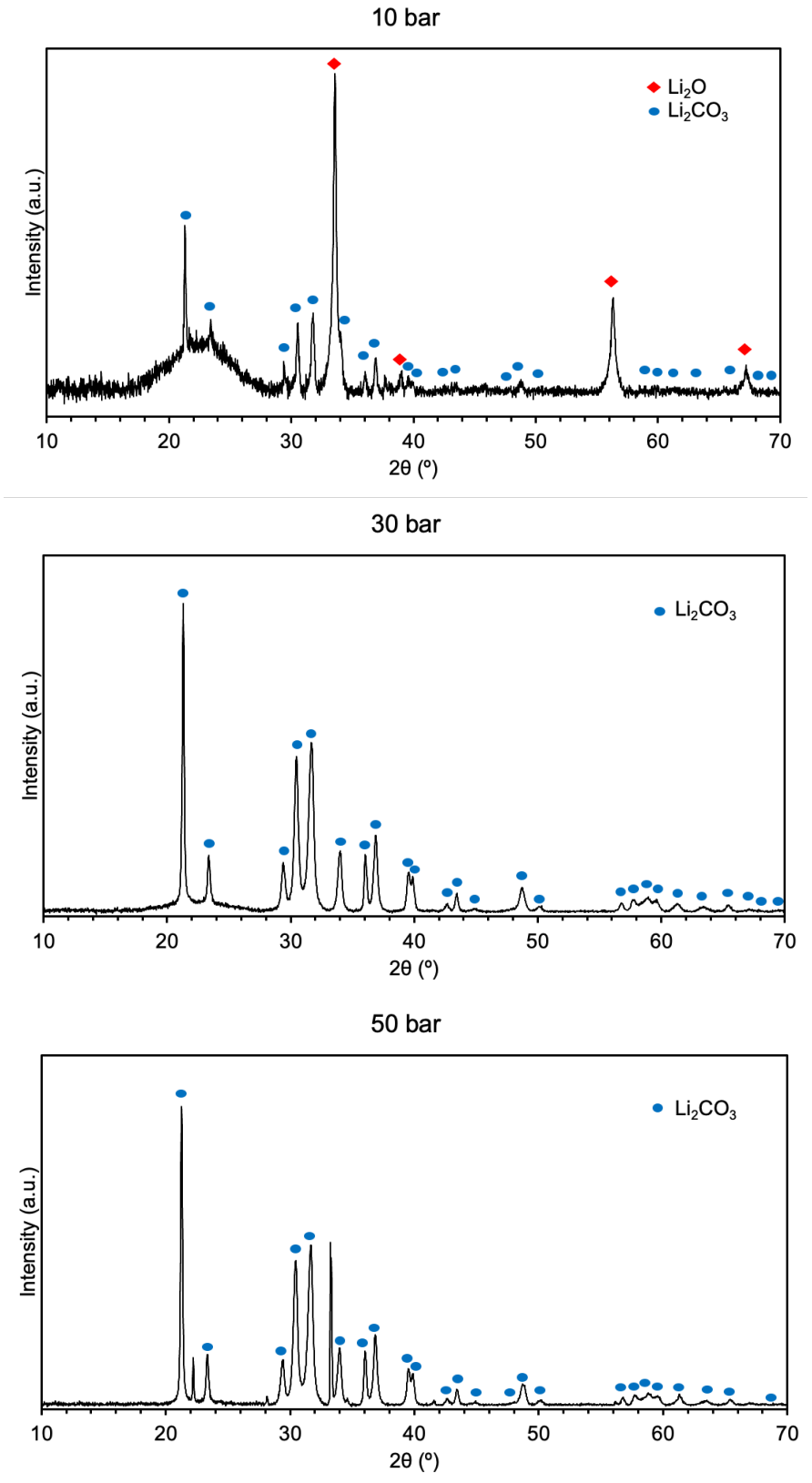

Figure 3.17: XRD patterns of the products of the Li-CO_2 reaction at 10, 30, and 50 bar.

Figure 3.18 shows the SEM images of the products obtained after the DSC tests at gauge pressures of 10 and 30 bar. Cracked spherical shells and compressed shells are seen in both images. Note that cracked shells were previously observed in the products obtained in the DSC tests at atmospheric pressure (see Figure 3.11a).

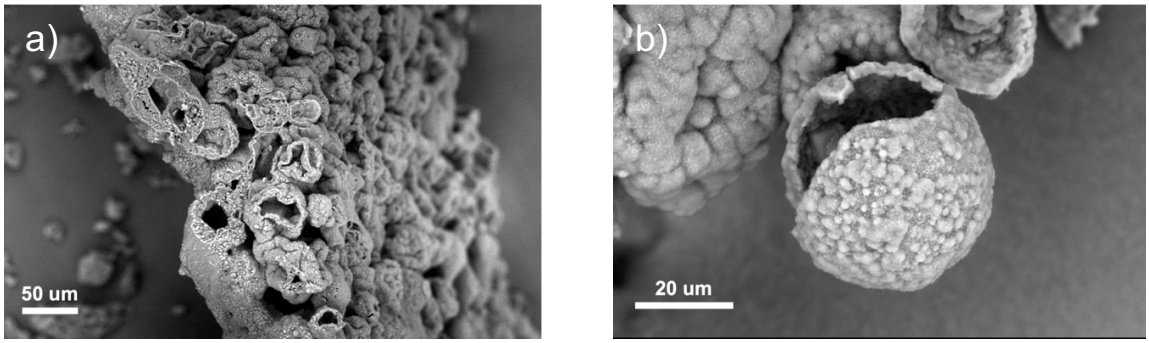

Figure 3.18: SEM images of the products of the Li-CO_2 reaction at (a) 10 and (b) 30 bar.

3.4. CONCLUSIONS

Oxidation of SLMP in an O_2/Ar environment has been studied by non-isothermal and isothermal TGA. The non-isothermal tests have shown a transition from the first stage to a faster second stage. The isothermal tests have revealed the formation of Li_2O_2 at temperatures below 400 °C, along with Li_2O. At higher temperatures, only Li_2O forms. The transition in the non-isothermal TGA curves is apparently caused by the decomposition of initially formed Li_2O_2. The oxidized particles are hollow shells, which implies that the oxidation process includes the growth of a solid oxide layer on the surface of the lithium droplet and the simultaneous growth of a cavity inside the droplet. The decomposition of Li_2O_2 changes the microstructure of the shell.

Combustion of SLMP in vertical quartz tubes with two open ends has been studied in a closed chamber filled with oxygen. Laser irradiation of the top surface of the sample results in vigorous combustion of the top layer accompanied by the motion of particles and formation of a gap near the bottom; then a counterflow combustion wave propagates downward. After this wave

has reached the bottom, the entire sample continues to emit light for a significant time. In some tests, a second (coflow) combustion wave propagated upward.

Non-isothermal TGA and DSC of SLMP in CO_2 flow have revealed a multi-stage process, which begins after melting of lithium. In the first stage, Li is fully oxidized to Li_2O, forming Li_2O/C shells. The second stage converts them into Li_2CO_3 shells. The overall reaction also forms C and CO byproducts. High-pressure DSC tests showed no effect of pressure on the peak temperature of the reaction of Li with CO_2, but XRD analysis revealed that full conversion to Li_2CO_3 at 30 and 50 bar occurs at a lower temperature than at 10 bar or atmospheric pressure.

No self-sustained combustion of SLMP was achieved in a CO_2 environment. Apparently, the formed products hinder the transport of CO_2.

Chapter 4: Conclusions

The combustion of Mg and Li powders in vertical quartz tubes at natural infiltration of oxygen has been demonstrated at atmospheric or lower pressure. It has been shown that laser ignition of magnesium powder at the top of the sample leads to a downward propagation of the counterflow combustion wave at low conversion followed by an upward propagation of the coflow combustion wave. The downward propagation of the coflow combustion wave immediately after the laser ignition does not occur because of sintering of the products during combustion of the top layer. Similarly, the ignition of lithium powder resulted in a downward propagation of the counterflow combustion wave, followed by either continued reaction of the entire sample or upward propagation of the coflow combustion wave. These results prove that a low Pilling-Bedworth ratio of Mg and Li (0.81 for Mg and 0.57 for Li) enables their coflow combustion with infiltrating oxygen. In CO_2, self-sustained combustion did not occur, apparently because of formation of impermeable product layers (MgO/C and Li_2CO_3/C) and CO, which hinder CO_2 transportation to the reaction zone.

Oxidation of stabilized lithium metal powder (SLMP) powder in O_2 and CO_2 has been investigated. In both cases, Li powder reacted after melting, leading to the formation of hollow spheres. Oxidation of Li powder by O_2 in non-isothermal tests have shown a transition from a slow to a faster stage. Isothermal tests revealed the formation and decomposition of Li_2O_2 causing the transition. Non-isothermal TGA and DSC of SLMP in CO_2 flow have revealed a multi-stage process. In the first stage, Li is fully oxidized to Li_2O, forming Li_2O/C shells. The second stage converts them into Li_2CO_3 shells. The overall reaction also forms C and CO byproducts. High-pressure DSC has shown that the increase in pressure from 10 to 30 bar promotes the conversion of the sample into Li_2CO_3.

References

[1] T.J. Hendricks, E.J. Brandon, R.L. Lam, D.E. Peterson, K.R. Anderson, B.C. Carroll, Chemical heat integrated power systems (CHIPS) to survive lunar night environments, 2020 Conference on Advanced Power Systems for Deep Space Exploration (2020).

[2] M. Hunter, K. Anderson, E. Brandon, D. Peterson, M. Pauken, W. West, Heat and electrical power for surviving the lunar night: the chemical heat integrated power source (CHIPS), 2022 Conference on Advanced Power Systems for Deep Space Exploration (2022).

[3] K.R. Anderson, E.J. Brandon, B. Carroll, T.J. Hendricks, M. Hunter, R. Lam, D. Peterson, W. West, Thermal systems modeling of chemical heat integrated power source (CHIPS) to survive lunar night environments, 50th International Conference on Environmental Systems (2021).

[4] C.J. Greer, J.A. Peters, M.P. Manahan, J.J. Cor, A.S. Rattner, Experimental characterization of lithium-carbon dioxide combustion in batch reactors for powering Venus landers, Acta Astronaut. 181 (2021) 235-248.

[5] S. Cordova, K. Estala-Rodriguez, E. Shafirovich, Oxidation kinetics of magnesium particles determined by isothermal and non-isothermal methods of thermogravimetric analysis, Combust. Flame 237 (2022) 111861.

[6] V.P. Kobyakov, V.M. Mal'tsev, L.B. Mashkinov, I.D. Chashechkin, Study of thermal waves in the gasless combustion of solid mixtures in a casing, Combust. Explos. Shock Waves 32 (1996) 432-435.

[7] V.P. Kobyakov, V.D. Zozulya, M.A. Sichinava, N.V. Sachkova, A.F. Belikova, D.Yu. Kovalev, Combustion of a Fe2O3-TiO2-Al-C powder mixture in the SHS regime and the structure of the combustion products, Combust. Explos. Shock Waves 41 (2005) 414-420.

[8] V.P. Kobyakov, D.Yu. Kovalev, Effect of heat release conditions on the phase composition of the combustion products of a Fe2O3/TiO2/Al/C thermite mixture, Combust. Explos. Shock Waves 44 (2008) 405-409.

[9] T.G. Hughes, R.B. Smith, D.H. Kiely, Stored chemical energy propulsion system for underwater applications, J. Energy 7 (1983) 128-133.

[10] T.F. Miller, M.V. Paul, S.R. Oleson, Combustion-based power source for Venus surface missions, Acta Astronaut. 127 (2016) 197-208.

[11] C.J. Greer, M.V. Paul, A.S. Rattner, Analysis of lithium-combustion power systems for extreme environment spacecraft, Acta Astronaut. 151 (2018) 68-79.

[12] J.W. Mausteller, Oxygen-generation systems, Kirk-Othmer Encyclopedia of Chemical Technology, Wiley, New York, NY, 2000.

[13] J. Graf, C. Dunlap, J. Haas, M. Weislogel, J. Lewis, K. Meyers, A. McKernan, Development of a solid chlorate backup oxygen delivery system for the International Space Station, International Conference on Environmental Systems (2000), SAE Technical Paper 2000-01-2348.

[14] A.G. Merzhanov, Historical retrospective of SHS: An autoreview, Int. J. Self-Propag. High-Temp. Synth. 17 (2008) 242-265.

[15] A. Varma, A.S. Rogachev, A.S. Mukasyan, S. Hwang, Combustion synthesis of advanced materials: Principles and applications, Adv. Chem. Eng. 24 (1998) 79-226.

[16] W.M. Haynes (Ed.), CRC Handbook of Chemistry and Physics, 94th ed., CRC Press, Boca Raton, 2013.

[17] M.W. Chase, Jr., NIST-JANAF Thermochemical Tables, 4st ed., J. Phys. Chem. Reference Data, Monograph 9 (1998) 1-1951.

[18] N.B. Pilling, R.E. Bedworth, The oxidation of metals at high temperatures, J. Inst. Met. 29 (1923) 529-591.

[19] A.P. Aldushin, A.G. Merzhanov, B.I. Khaikin, Conditions for the layer filtration combustion of porous metals, Dokl. Phys. Chem. 215 (1974) 295-298.

[20] A.P. Aldushin, T.P. Ivleva, A.G. Merzhanov, B.I. Khaikin, K.G. Shkadinskii, Combustion front propagation in porous exothermic metallic samples with oxidizer filtration, in: A.G. Merzhanov (Ed.), Protsessy Goreniya v Khimicheskoi Tekhnologii i Metallurgii (Combustion Processes in Chemical Technology and Metallurgy), Izd. Inst. Khim. Fiz., Chernogolovka, 1975, pp. 245-252.

[21] A.P. Aldushin, Filtration combustion of metals, in: Y.S. Matros (Ed.), Rasprostranenie Teplovykh Voln v Geterogennykh Sredakh (Propagation of Heat Waves in Heterogeneous Media), Nauka, Novosibirsk, 1988, pp. 52-71.

[22] A.P. Aldushin, B.S. Seplyarskii, K.G. Shkadinskii, Theory of filtrational combustion, Combust. Explos. Shock Waves 16 (1980) 33-40.

[23] K.G. Shkadinsky, G.V. Shkadinskaya, B.J. Matkowsky, V.A. Volpert, Two-front traveling waves in filtration combustion, SIAM J. Appl. Math. 53 (1993) 128-140.

[24] A.P. Aldushin, New results in the theory of filtration combustion, Combust. Flame 94 (1993) 308-320.

[25] A.P. Aldushin, I.E. Rumanov, B.J. Matkowsky, Maximal energy accumulation in a superadiabatic filtration combustion wave, Combust. Flame 118 (1999) 76-90.

[26] T.P. Ivleva, A.G. Merzhanov, Spinning waves of infiltration-mediated combustion, Int. J. Self-Propag. High-Temp. Synth. 17 (2008) 157-167.

[27] T.P. Ivleva, A.G. Merzhanov, Effect of gas pressure on the laws of propagation of spinning waves during filtration combustion, Combust. Explos. Shock Waves 45 (2009) 534-542.

[28] A.N. Pityulin, V.A. Shcherbakov, I.P. Borovinskaya, A.G. Merzhanov, Laws and mechanism of diffusional surface burning of metals, Combust. Explos. Shock Waves 15 (1979) 432-437.

[29] M.A. Machado, D.A. Rodriguez, Y. Aly, M. Schoenitz, E.L. Dreizin, E. Shafirovich, Nanocomposite and mechanically alloyed reactive materials as energetic additives in chemical oxygen generators, Combust. Flame 161 (2014) 2708-2716.

[30] D.A. Rodriguez, E.L. Dreizin, E. Shafirovich, Hydrogen generation from ammonia borane and water through combustion reactions with mechanically alloyed Al·Mg powder, Combust. Flame 162 (2015) 1498-1506.

[31] S.E. Guerrero, E.L. Dreizin, E. Shafirovich, Combustion of thermite mixtures based on mechanically alloyed aluminum-iodine material, Combust. Flame 164 (2016) 164-166.

[32] R.E. Ferguson, E. Shafirovich, Aluminum-nickel combustion for joining lunar regolith ceramic tiles, Combust. Flame 197 (2018) 22-29.

[33] A.P. Aldushin, B.A. Malomed, Ya.B. Zeldovich, Phenomenological theory of spin combustion, Combust. Flame 42 (1981) 1-6.

[34] A.K. Filonenko, Spin combustion of titanium at reduced pressure, Combust. Explos. Shock Waves 27 (1991) 685-689.

[35] A.K. Filonenko, V.V. Barzykin, The effect of density on the limits and regularities of spin combustion of titanium in nitrogen, Combust. Explos. Shock Waves 32 (1996) 45-49.

[36] A.K. Filonenko, Some characteristics of a spin combustion site and of the processes occurring in it. Combust. Explos. Shock Waves 34 (1998) 288-291.

[37] A.S. Mukasyan, S.G. Vadchenko, I.O. Khomenko, Combustion modes in the titanium-nitrogen system at low nitrogen pressures, Combust. Flame 111 (1997) 65-72.

[38] A.S. Mukasyan, J.A. Marasia, I.A. Filimonov, A. Varma, Role of infiltration in spin combustion in gas–solid systems, Combust. Flame 122 (2000) 368-374.

[39] M. Wolff, T. Ebel, M. Dahms, Sintering of magnesium, Adv. Eng. Mater. 12 (2010) 829-836.

[40] A.A. Shiryaev, Thermodynamics of SHS processes: Advanced approach, Int. J. Self-Propag. High-Temp. Synth. 4 (1995) 351-362.

[41] E.I. Gusachenko, L.N. Stesik, V.P. Fursov, V.I. Shevtsov, Investigation of the condensed combustion products of magnesium powders I. Dependence on pressure, Combust. Explos. Shock Waves 10 (1974) 476-482.

[42] E.I. Gusachenko, L.N. Stesik, V.P. Fursov, V.I. Shevtsov, Investigation of the condensed combustion products of magnesium powders II. Dependence on particle size, Combust. Explos. Shock Waves 10 (1974) 588-595.

[43] V.V. Grachev, R.V. Solov'ev, Two-dimensional model of infiltration-mediated combustion: Effect of heat losses, Int. J. Self-Propag. High-Temp. Synth. 16 (2007) 105-109.

[44] E. Shafirovich, A.S. Mukasyan, A. Varma, G. Kshirsagar, Y. Zhang, J.C. Cannon, Mechanism of combustion in low-exothermic mixtures of sodium chlorate and metal fuel, Combust. Flame 128 (2002) 133-144.

[45] S. Cordova, K. Estala-Rodriguez, E. Shafirovich, Infiltration-controlled combustion of magnesium for power generation in space, Combust. Flame, 238 (2022) 111950.

[46] Y. Li and B. Fitch, Effective enhancement of lithium-ion battery performance using SLMP, Electrochem. Comm. 13 (2011) 664-667.

[47] A basic laboratory safe handling guide for stabilized lithium metal powder (SLMP®) and SLMP product variants, Livent, available at <https://livent.com/wp-content/uploads/2018/10/SLMP-Safe-Handling-Guide-v10.09.18.pdf>.

[48] B. Xiang, L. Wang, G. Liu, A.M. Minor, Electromechanical probing of Li/Li2CO3 core/shell particles in a TEM, J. Electrochem. Soc. 160 (2013) A415-A419.

[49] J.T. Vaughey, G. Liu, J.-G. Zhang, Stabilizing the surface of lithium metal, MRS Bull. 39 (2014) 429-435.

[50] P. Fischer, M. Schiemann, V. Scherer, P. Maas, G. Schmid, D., Taroata, Experimental characterization of the combustion of single lithium particles with CO2, Fuel 153 (2015) 90-101.

[51] M. Schiemann, J. Bergthorson, P. Fischer, V. Scherer, D. Taroata, G. Schmid, A review on lithium combustion, Appl. Energy 162 (2016) 948-965.

[52] Yu.A. Ferapontov, N.V. Kokoreva, N.P. Kozlova, M.A. Ul'yanova, Thermal analysis of lithium peroxide prepared by various methods, Russ. J. Gen. Chem. 79 (2009) 891-894.

[53] H. Beyer, S. Meini, N. Tsiouvaras, M. Piana, H.A. Gasteiger, Thermal and electrochemical decomposition of lithium peroxide in non-catalyzed carbon cathodes for Li–air batteries, Phys. Chem. Chem. Phys. 15 (2013) 11025.

[54] J. Kim, H. Kang, K. Hwang, S. Yoon, Thermal decomposition study on Li2O2 for Li2NiO2 synthesis as a sacrificing positive additive of lithium-ion batteries, Molecules 24 (2019) 4624.

[55] G.J. Janz, M.R. Lorenz, Equilibrium dissociation pressures of molten lithium carbonate, J. Chem. Eng. Data 9 (1964) 94-95.

[56] H.A. Mosqueda, C. Vazquez, P. Bosch, H. Pfeiffer, Chemical sorption of carbon dioxide (CO2) on lithium oxide (Li2O), Chem. Mater. 18 (2006) 2307-2310.

Appendix

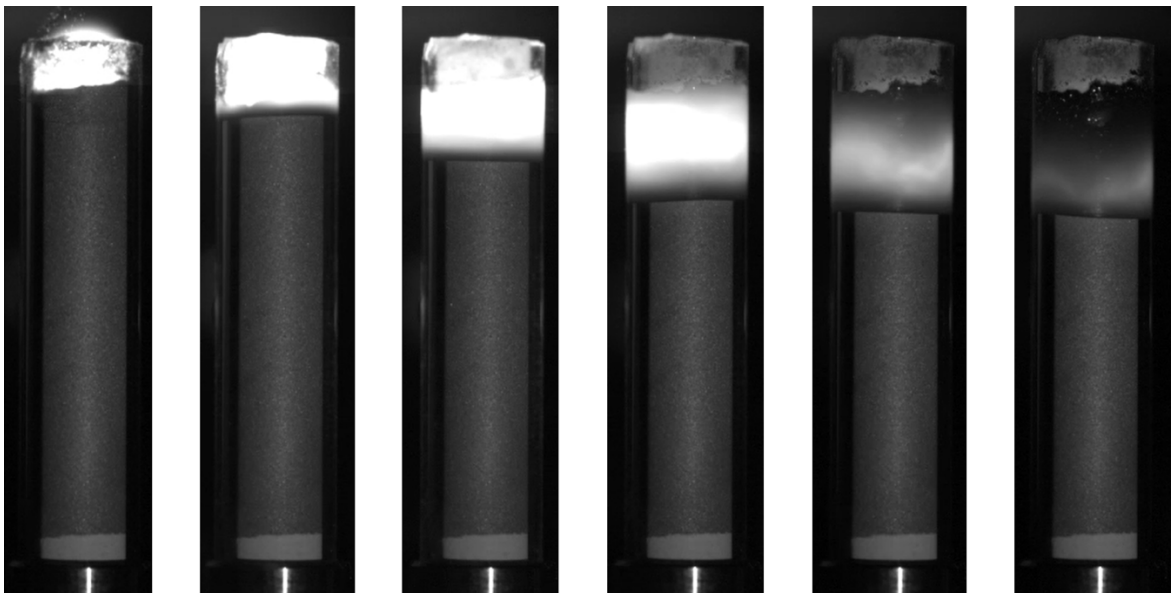

Figure A1: Combustion of Mg powder in oxygen at 90 kPa. Bottom end sealed with ceramic paste.

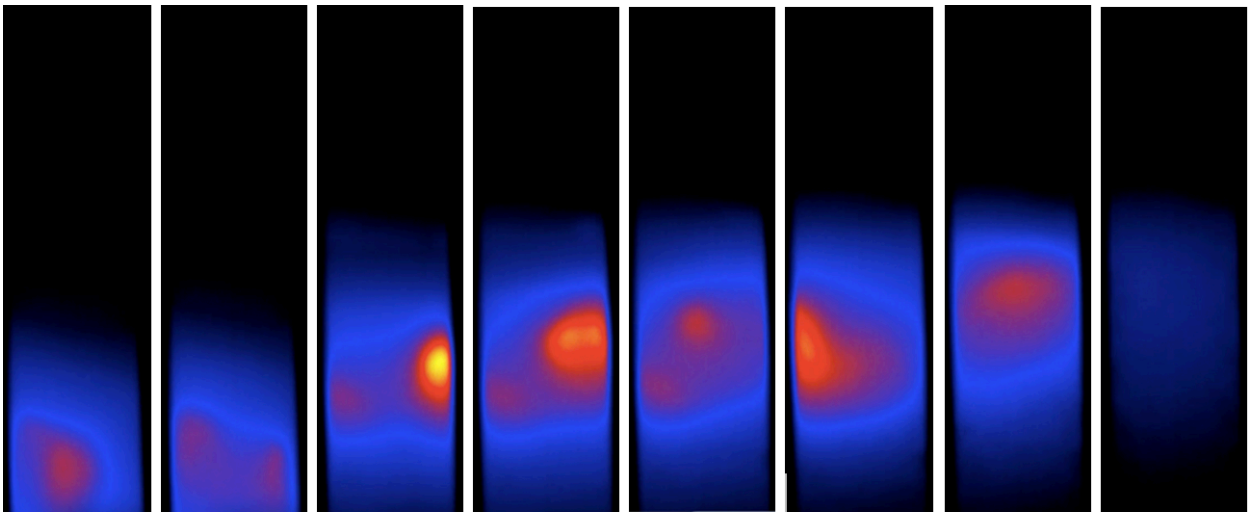

Figure A2: Hot spots captured by infrared recording during upward combustion of Mg and O_2. Images of video recording section of 26 s.

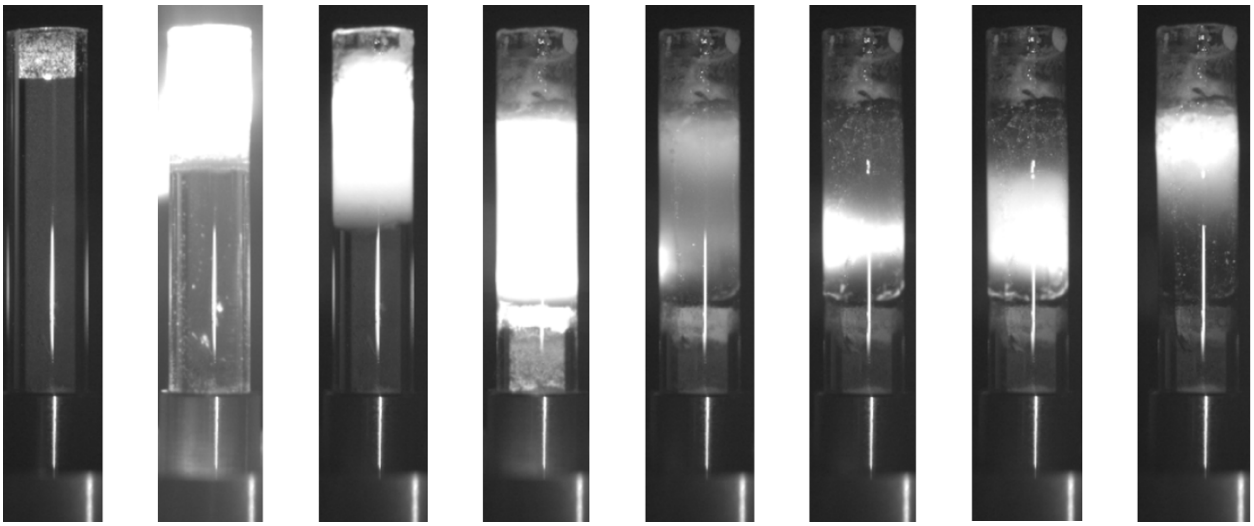

Figure A3: Combustion of Li powder in oxygen at 90 kPa with upward combustion wave.

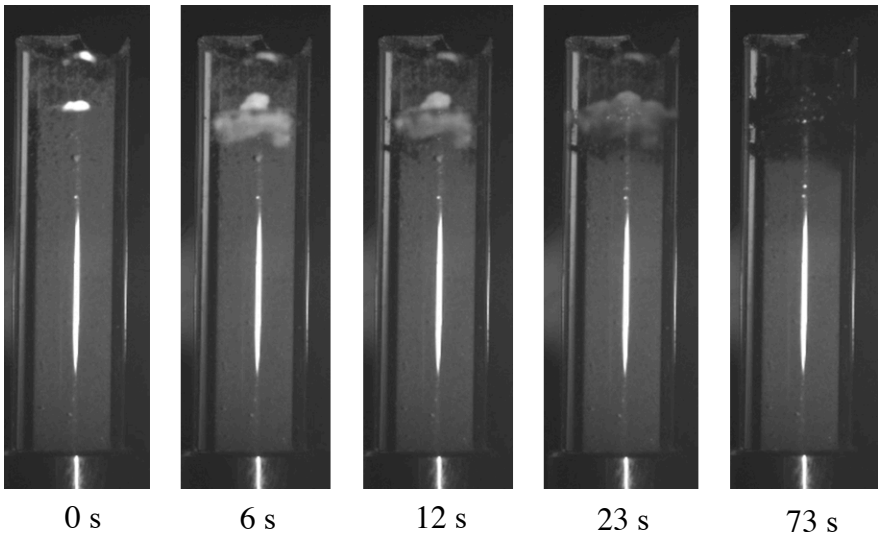

Figure A4: Combustion of Li in CO_2 at 90 kPa. Time relative to laser pulse.

Vita

Kevin Samuel Estala Rodriguez received his A.S. in Mechanical Engineering from El Paso Community College in 2016. He transferred to the University of Texas at El Paso (UTEP) where he obtained his B.S. (Magna Cum Laude) and M.S. in Mechanical Engineering in 2018 and 2022, respectively. He also obtained a 3D Engineering and Additive Manufacturing Certificate in 2020.

In Spring of 2020, Kevin started his PhD studies in Dr. Shafirovich's research team at UTEP on a project for the combustion of metal fuels for space power systems, supported by an Early Stage Innovations grant from NASA's Space Technology Research Grants Program. In 2021, Kevin attended the Summer Combustion School in Princeton University. In summer 2022, he conducted research on metal combustion at McGill University in Montreal, Canada, supported by the U.S. National Science Foundation.

Kevin has coauthored three peer-reviewed journal articles. Two articles have been published in *Combustion and Flame* and one in *Proceedings of the Combustion Institute*. His work has been presented in several national and international conferences including the 39th International Symposium on Combustion (Vancouver, Canada), 2022 Conference on Advanced Power Systems for Deep Space Exploration (Virtual), 2022 Spring Technical Meeting of the Central States Section of the Combustion Institute (Detroit, MI), and the 1st Workshop on Metal-enabled Cycle of Renewable Energy (Eindhoven, The Netherlands). His travel to the 39th International Symposium on Combustion was supported by the U.S. National Science Foundation and the Combustion Institute.

Contact Information: kestalarod@miners.utep.edu